

# 1SXPS: A DEEP SWIFT X-RAY TELESCOPE POINT SOURCE CATALOG WITH LIGHT CURVES AND SPECTRA

P.A. EVANS, J.P. OSBORNE, A.P. BEARDMORE, K.L. PAGE, R. WILLINGALE, C.J. MOUNTFORD, C. PAGANI  
University of Leicester, X-ray and Observational Astronomy Group, Department of Physics and Astronomy, University Road, Leicester,  
LE1 7RH, UK

D.N. BURROWS AND J.A. KENNEA  
Department of Astronomy and Astrophysics, Pennsylvania State University, University Park, Pennsylvania 16802, USA

M. PERRI  
ASI-Science Data Center, Via del Politecnico, I-00133 Rome, Italy  
INAF-Osservatorio Astronomico di Roma, Via Frascati 33, I-00040 Monteporzio Catone, Italy

G. TAGLIAFERRI  
INAF Osservatorio Astronomico di Brera, via E. Bianchi 46, 23807 Merate (LC), Italy

AND

N. GEHRELS  
NASA/Goddard Space Flight Center, Greenbelt, MD 20771, USA

*Draft version November 7, 2018*

## ABSTRACT

We present the 1SXPS (Swift-XRT Point Source) catalog of 151,524 X-ray point-sources detected by the *Swift*-XRT in 8 years of operation. The catalog covers 1905 square degrees distributed approximately uniformly on the sky. We analyze the data in two ways. First we consider all observations individually, for which we have a typical sensitivity of  $\sim 3 \times 10^{-13}$  erg cm<sup>-2</sup> s<sup>-1</sup> (0.3–10 keV). Then we co-add all data covering the same location on the sky: these images have a typical sensitivity of  $\sim 9 \times 10^{-14}$  erg cm<sup>-2</sup> s<sup>-1</sup> (0.3–10 keV). Our sky coverage is nearly 2.5 times that of 3XMM-DR4, although the catalog is a factor of  $\sim 1.5$  less sensitive. The median position error is 5.5'' (90% confidence), including systematics. Our source detection method improves on that used in previous XRT catalogs and we report > 68,000 new X-ray sources. The goals and observing strategy of the *Swift* satellite allow us to probe source variability on multiple timescales, and we find  $\sim 30,000$  variable objects in our catalog. For every source we give positions, fluxes, time series (in four energy bands and two hardness ratios), estimates of the spectral properties, spectra and spectral fits for the brightest sources, and variability probabilities in multiple energy bands and timescales.

*Subject headings:* Catalogs – Surveys – X-rays: general – Methods: data analysis

## 1. INTRODUCTION

Serendipitous X-ray source catalogs have been produced for most X-ray satellites since the *Einstein* mission (e.g. Gioia et al. 1990; Voges et al. 1999; Ueda et al. 2005; Watson et al. 2009; Evans et al. 2010) and have contributed much to our understanding of the X-ray sky. The *Swift* satellite (Gehrels et al. 2004) has several unique features which mean that a serendipitous source catalog produced from its X-ray Telescope (XRT; Burrows et al. 2005) can make a distinctive contribution to this field, particularly in the area of source variability. To make this catalog we have analyzed *Swift*-XRT data from the first 8 years of operations, covering 13,065 distinct locations (giving a coverage of 1905 square degrees), of which 81% were observed at least twice. In many cases a field is observed both multiple times within a day, and over a period of many days, allowing us to probe variability on different timescales. Swift pointings have been performed across the entire sky with considerable unifor-

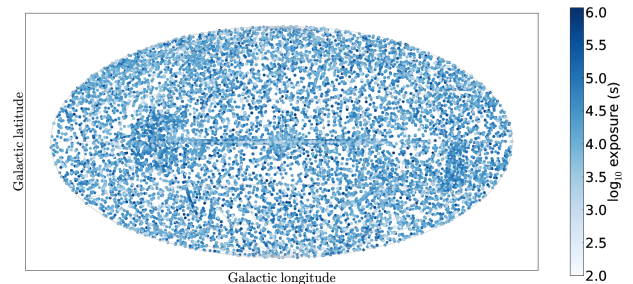


**Figure 1.** The locations of the observations in the 1SXPS catalog in Galactic coordinates. The colors of the points indicate the exposure time included in the catalog. The point sizes are larger than the XRT field of view. A color version of this figure is available in the electronic version of the paper.

mity, although there is an over-density of pointings along the Galactic plane; see Fig. 1.

The XRT contains a CCD detector with a bandpass of 0.3–10 keV, with a peak effective area of 110 cm<sup>2</sup> at 1.5 keV. The field of view has a radius of 12.3', with

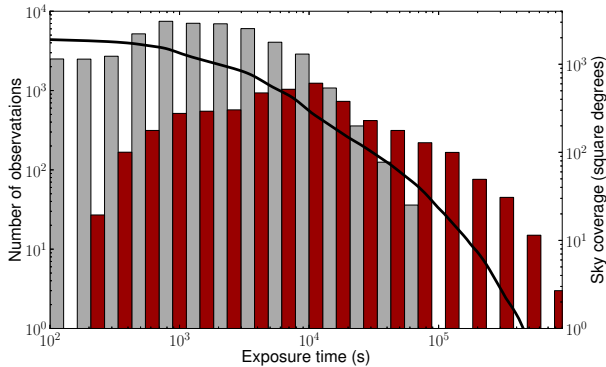


**Figure 2.** Temporal and geometric coverage of the 1SXPS catalog. The solid line shows the unique sky coverage of the catalog as a function of exposure time. The histogram shows the distribution of exposure times of the observations (gray) and the stacked images (black; red in the electronic version).

vignetting at the outer edge reducing the effective area by  $\sim 25\%$  (at 1.5 keV); there are also several detector columns permanently masked out due to damage from a micrometeoroid impact of 2005 May 27 (Abbey et al. 2006).

Two previous XRT point-source catalogs have been produced, which used the routines built into the XIMAGE software to detect sources. The first, Puccetti et al. (2011), analyzed the deepest GRB fields, combining all of the data into a single image per field. The second, D’Elia et al. (2013), analyzed 7 years of XRT data, considering each observation independently. For this catalog we have developed a new detection method capable of detecting fainter sources than these papers, and have conducted a rigorous analysis of our completeness and false positive rate; we have also considered both individual observations and deep images, making this a more complete point source catalog than those of Puccetti et al. (2011) and D’Elia et al. (2013). We have produced light curves and variability estimates for every source detected in the catalog. These are available through a dedicated website.

We performed our analysis in four energy bands: one covering the entire calibrated energy range of the XRT (0.3–10 keV), and three partial bands which were chosen to overlap those used in the 2XMM catalog (Watson et al. 2009); these are listed in Table 1. For a typical AGN spectrum this will give approximately the same number of events in each of the three partial bands. Summary details of the catalog are given in Table 1.

This paper is organized as follows: In Section 2 we discuss the data selection and filtering applied before collating the catalog. In Section 3 we detail the analysis process, the results of which are given in Section 4. In Section 5 we demonstrate the reliability of our catalog compilation, while Section 6 discusses the false positive rate and completeness.

### 1.1. Data timescales: snapshots, observations and stacked images

*Swift* data are organized into *snapshots* and *observations*. Due to its low Earth orbit ( $P=96$  min), *Swift* cannot observe an object continuously for more than 2.7 ks, thus most observations are spread over multiple spacecraft orbits. A single, continuous on-target exposure is

referred to as a *snapshot*. Within a UT day<sup>1</sup>, the data from all snapshots pointed at a given source are aggregated into a single dataset, referred to as an *observation* and is assigned a unique *ObsID* under which the data can be accessed. In order to probe source variability we consider both of these timescales. Neither snapshots nor observations have a standard duration: snapshots may be 300–2700 s in duration<sup>2</sup> and there are typically 1–15 snapshots in an observation. However snapshot-to-snapshot variability probes timescales  $<1$  day, while observation to observation variability probes timescales  $>1$  day.

Snapshots are generally too short for any but the brightest sources to be detected, therefore we search for sources in each observation and on summed images comprising all XRT observations on each location of the sky. We refer to these latter as *stacked images*. The word *image* where it appears in this paper can be taken literally as a single (FITS) image, which may be of a snapshot, observation or a stacked image; whereas *field* refers to an area on the sky. Fig. 2 shows the distribution of exposure times in the two types of image on which we perform source detection, and the sky coverage of the catalog as a function of exposure time.

## 2. DATA SELECTION

Initially we selected every XRT science observation<sup>3</sup> collected before 2012 October 12 containing at least 100 s of Photon Counting (PC) mode data<sup>4</sup>; we also required that at least one snapshot in the observation was at least 100 s in duration. We removed any observations which overlap the locations listed in Table 2, as these include large-scale diffuse emission (identified by examining the XRT images) which is not well handled by our point-source-optimized detection system. We then filtered the remaining event lists to remove time intervals where the data were affected by light reflected off the sunlit Earth, or where the astrometry was unreliable (both described below); if this reduced the exposure time to below the 100-s limit, the observation was discarded.

### 2.1. Bright Earth filtering

When *Swift* points close to the Earth limb, at certain spacecraft roll angles the background level in the XRT is increased by contamination from light scattered off the sunlit side of the Earth. This is always most notable on the left-hand side of the detector. For each observation we therefore examined the raw event list (before the XRT-PIPELINE script has been executed) and selected events in a box  $122 \times 350$  pixels in size, centered on the XRT detector pixel (62, 300) (i.e. the left hand side). Times where the event rate in this box exceeds  $40 \text{ event s}^{-1}$  were deemed to be affected by bright Earth, and were removed from the observation before further processing. For 90% of the observations in our catalog, this removed less than 10% of the exposure time.

<sup>1</sup> i.e. from 00:00:00 to 23:59:59 UT.

<sup>2</sup> Shorter snapshots are possible if a Gamma Ray Burst interrupts the planned observations.

<sup>3</sup> Excluding ObsIDs beginning with ‘006’, as these are calibration datasets, sometimes taken in non-standard operating modes.

<sup>4</sup> Windowed Timing mode data have only 1-D spatial resolution so are inappropriate for detecting and localizing sources.

**Table 1**  
Summary details of the catalog

Category	Units	Value
Energy Bands:	keV	Total = $0.3 \leq E \leq 10$ Soft = $0.3 \leq E < 1$ Medium = $1 \leq E < 2$ Hard $2 \leq E < 10$
Sky Coverage	square degrees	1905
Median sensitivity (0.3–10 keV)	erg cm <sup>-2</sup> s <sup>-1</sup>	$3 \times 10^{-13}$
Number of detections		585,443
Number of unique sources		151,524
Number of variable sources		28,906
Number of uncataloged sources <sup>1</sup>		68,638

**Note.** — <sup>1</sup>i.e. without a match within  $3\text{-}\sigma$  in any of the catalogs detailed in Section 4.3 excluding the 2MASS and USNO-B1 catalogs.

**Table 2**  
Locations excluded from the catalog due to large-scale emission structures

RA deg, J2000	Dec deg, J2000	Identity
6.334	64.136	Tycho SNR
16.006	-72.032	SNR B0102-72.3
28.197	36.153	RSCG15
44.737	13.582	ACO 401
49.951	41.512	NGC 1275
81.510	42.942	Swift J0525.8+4256
83.633	22.014	Crab Nebula
83.867	-69.270	SN 1987A
85.052	-69.331	PSR 0540-69
94.277	22.535	OFGL J0617.4+2234
116.882	-19.303	PKS 0745-191
125.851	-42.781	Pup A
139.527	-12.100	Hydra A
161.017	-59.746	Carina Nebula
177.801	-62.626	ESO 130-SNR001
187.709	12.387	M87
194.939	27.943	Coma Cluster
207.218	26.590	Abell 1795
227.734	5.744	Abell 2029
229.184	7.020	Abell 2052
234.798	-62.467	Swift J1539.2-6227
239.429	35.507	Abell 2141
244.405	-51.041	SNR G332.4-00.4
258.116	-23.367	Ophiuchi Cluster
266.414	-29.012	Galactic Center
299.868	40.734	3C405.0
326.170	38.321	Cyg X-2
345.285	58.877	1E2259+586
350.850	58.815	Cas A

**Note.** — Observations within  $12.5'$  of these locations are excluded from our catalog.

## 2.2. Astrometry filtering

The standard astrometric calibration of XRT data is taken from the *Swift* star trackers, mounted on the XRT. This provides a solution which is accurate to  $3.5''$  90% of the time (Moretti et al. 2007). We identified and removed times where this astrometry was incorrect by more than  $10''$  by using the UV/Optical telescope (UVOT) on *Swift*. For each UVOT image we corrected the astrometry by matching UVOT sources to the USNO-B1 catalog. We then determined the magnitude of this correction on the X-ray sources in the image and at four locations positioned symmetrically in the field at radii of  $5.9'$  from the

field center (i.e. mid-way to the edge of the field). This was done using the known translation from the UVOT detector to the XRT detector, as described in Goad et al. (2007). If any of these corrections were  $>10''$  we marked the times of that UVOT image as bad and excluded XRT data taken during those times from the analysis. This was implemented as a two-pass process, since it makes use of the XRT source list for a given observation, which was not produced until the entire detection system had completed. We therefore ran the detect procedure on the per-observation timescale in full without this phase before performing this astrometric check. Any observations identified by this process were then reanalyzed from scratch, with the times of poor astrometry removed. The stacked images were only created and processed after this had been completed.

## 3. DATA PROCESSING

For all analysis in this catalog we used the HEASOFT version 6.12 software which includes the XRTDAS v2.8.0 developed at the ASI Science Data Center (ASDC, Italy), and the XRT CALDB version 20120209. Event files were reprocessed using the XRTPIPELINE task with the standard filtering criteria to provide a self-consistent and up-to-date set of event lists.

### 3.1. Stacked image creation

Our source detection software works in the SKY ( $x, y$ ) coordinate system, which is a virtual system constructed using a tangent plane projection such that  $(x, y)$  has a linear mapping to (RA, Dec) (see Greisen & Calabretta 2002; Calabretta & Greisen 2002). This coordinate system is produced uniquely for each ObsID when XRTPIPELINE is run. For the stacked images we therefore used the COORDINATOR FTOOL to reconstruct the coordinates for all observations within a stacked image using the same projection.

There is a small number of locations on the sky (4% of those covered by our catalog) where overlapping observations exist that extend beyond the  $1000 \times 1000$  pixel ( $=39.9' \times 39.3'$ ) range of the SKY coordinates in the XRT event files and thus could not be covered by a single stacked image. In these cases we split the observations into multiple stacked images, aiming to minimize the sky area lost while maximizing depth of exposure.

For stacked images of GRB fields we excluded the first snapshot of data from the stacked image as the GRB

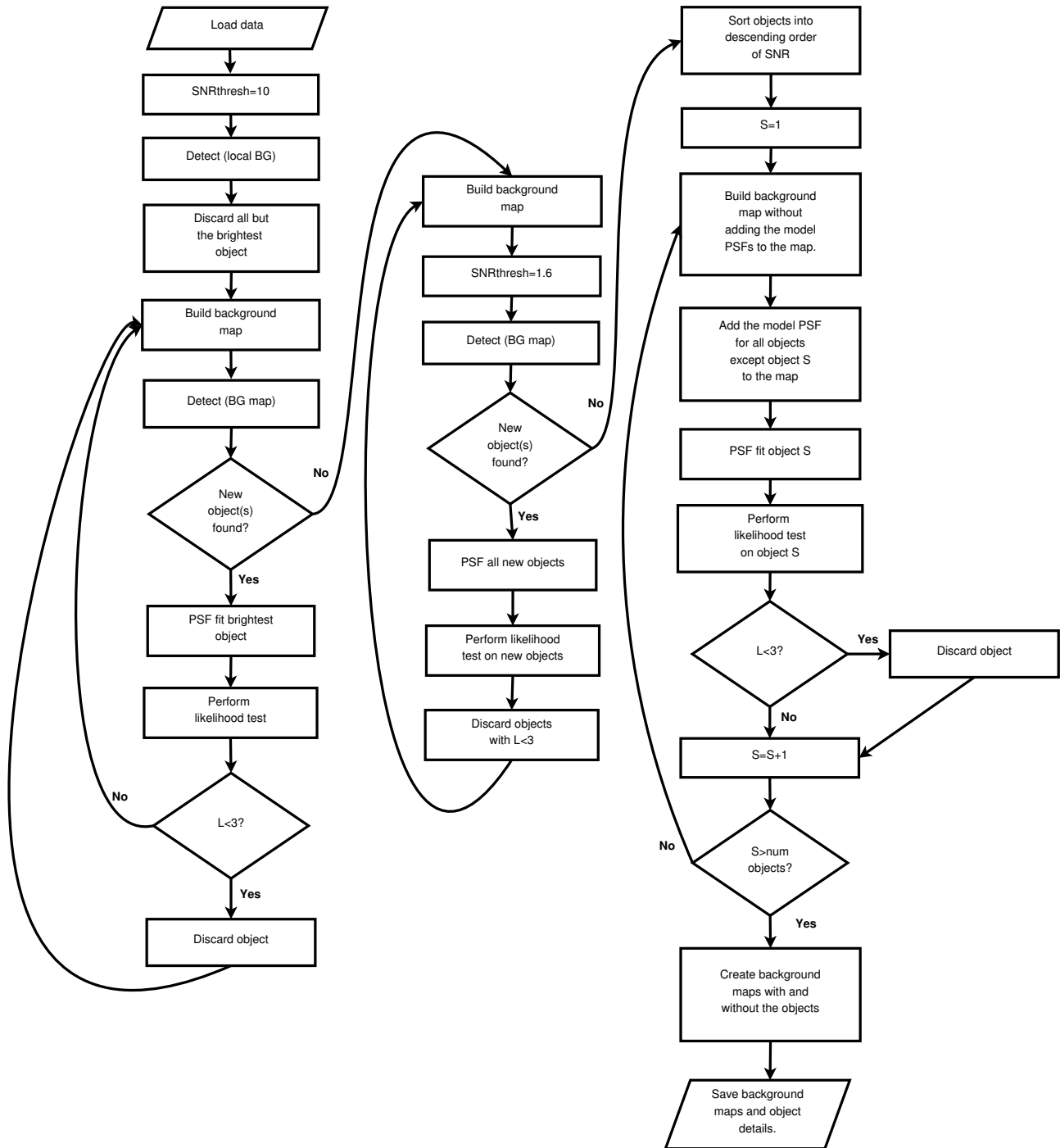


**Figure 3.** Flowchart showing the source detection and characterization algorithm.

tends to be bright at this time which would reduce the sensitivity to fainter sources in the image.

From this point onwards the process followed was the same for stacked images and single observations<sup>5</sup>, and the phrase ‘dataset’ refers to either of these.

### 3.2. Data preparation

<sup>5</sup> With the exception that, for stacked images the data preparation phase is carried out for multiple event lists, once per observation in the image.

Source detection was performed on a single image (in each band) which contained all of the usable (Section 2) exposure time in that dataset. However the background maps had to be created on a per-snapshot basis and then combined to give the full map (see Section 3.3.2 for details). The datasets were therefore split into snapshots, and for each snapshot an exposure map was created (which included the effects of vignetting, assuming an event energy of 1.5 keV which is where the XRT effective area is at its highest) and an image was constructed of the grade 0-12 events in each of the four energy bands (Ta-

ble 1). The center of the image and the mean spacecraft roll angle for that snapshot were recorded to be used by the background-mapping software. The XRT has three different window sizes that have been used at different times:  $480 \times 480$  pixels,  $500 \times 500$  pixels, and  $600 \times 600$  pixels; the size that was used was also recorded. Finally, the per-snapshot exposure maps were summed to give a single, total exposure map (as well as the per snapshot maps) as were the images in each energy band. These files were then passed to the source detection software.

### 3.3. Source Detection

Source detection was performed independently for each energy band. We used a form of sliding-cell detection combined with a fit to the point spread function (PSF) to identify, localize and characterize sources. Our approach is based on that employed for the 2XMM catalog (Watson et al. 2009), optimized for *Swift*-XRT data. The algorithm is composed of the following elements:

1. Sliding-cell detection with a locally-estimated background
2. Creation of a background map
3. Sliding-cell detection using the background map
4. Source characterization using a PSF fit
5. Likelihood testing

The source detection process is non-linear and iterative. The specific details (e.g. thresholds) and ordering of the steps were optimized through a series of trials and simulations. An overview of the algorithm is given in the rest of this section; the components of that algorithm are detailed in the following sections.

A flow-chart depicting the source-detection algorithm is shown in Fig. 3. The initial step was a sliding-cell detection with a locally estimated background. The source list thus produced was required only to produce the initial background map and only needs to identify the brightest sources. We therefore used a signal-to-noise (SNR) threshold of 10. Only the brightest source was considered, and this was only used to create a background map, and then discarded. A second sliding-cell detection was then performed, this time using the background map. The SNR threshold at this point was still 10, and only the single brightest source detected was kept. This is necessary to avoid detecting artifacts around bright sources. If a source was detected at this point, the PSF was fitted to the source and a likelihood test was performed. If the likelihood value (Section 3.3.5) was below 3, the source was discarded as spurious; its position was noted so that, if the object were redetected in a later step, it could be immediately discarded. The background map was then rebuilt, and the model PSF of the detected source was added to the map, which reduces the probability of detecting the artifacts just alluded to (see Section 3.3.2 for details). The sliding-cell detection using the background map, and subsequent steps, were then repeated until no new objects were detected. These steps correspond to the left-hand column in Fig. 3.

The detection threshold was then reduced to  $\text{SNR}=1.6$  and the process continued largely as above (build background map, detect, PSF fit; repeat) except that *all* objects detected were passed to the PSF fit, rather than just the brightest one. This was repeated until no new objects were found. This stage is represented by the central column of Fig. 3.

The final stage of the process was to perform a new PSF fit and likelihood test for each object detected. This was needed because because the initial steps carried out above were done before all of the objects had been detected, so the background map will have evolved since this time. We therefore created the background map, adding in the model PSFs of all but the highest SNR object. We then performed the PSF fit and likelihood test on the highest SNR object, using this map. This process was then repeated with the second-highest SNR object left out of the map (the highest SNR source, relocalized in the previous iteration, is included) and the PSF fit and likelihood tests performed for that source, and so on through each source. Finally, two definitive background maps were created and saved: one containing only the background, one also including the model PSF of every object detected. These steps are shown in the right-hand column of Fig. 3.

We will now describe the five principle components of this process.

#### 3.3.1. Sliding-cell detection with a locally-estimated background

Use of a locally-estimated background was made only once in our process. During this phase the SNR threshold for a detection was 10. The algorithm employed was that detailed in the *Chandra Detect* Reference Manual<sup>6</sup>. We used a  $21 \times 21$  pixel ( $=49.5''$ ) cell and stepped it over the entire image in steps of 7 pixels. For each step, we measured the number of events,  $C$  in the cell. The error was calculated according to the Gehrels (1986) formula:

$$\sigma_C = 1.0 + \sqrt{C + 0.75} \quad (1)$$

which approximates the Poisson distribution better than  $\sqrt{C}$  for low values of  $C$ .

We also measured the number of events,  $T$  in a cell of size  $51 \times 51$  pixels with the same central position as the source. If the real number of background events in the inner cell is  $B$ , and the number contributed by a source at the center of that cell is  $S$ , then:

$$C = \alpha S + B \quad (2)$$

$$T = \beta S + \left(\frac{b}{d}\right)^2 B \quad (3)$$

where  $\alpha = 0.814$  and  $\beta = 0.937$  are the fraction of source counts expected in the inner and outer cell respectively, determined from the PSF of XRT Moretti et al. (2007);  $d = 21$  and  $b = 51$  pixels are the widths of the inner and outer cells.

<sup>6</sup> [http://asc.harvard.edu/ciao/download/doc/detect\\_manual/cell\\_theory.html](http://asc.harvard.edu/ciao/download/doc/detect_manual/cell_theory.html)

Solving for  $B$  and then  $S$  gives the SNR in the inner cell:

$$\text{SNR} = \frac{S}{\sigma_S} = \frac{C(b^2 - d^2)d^{-2} - Q}{\sqrt{\sigma_C^2(b^2 - d^2)^2 d^{-4} + \sigma_Q^2}} \quad (4)$$

where

$$Q = T - C \quad (5)$$

This implicitly assumes that the exposure is constant across both the inner and outer cell, which may not be true. Therefore to determine  $Q$ , we measured the number of counts that were in the outer cell but not the inner cell, and then multiplied this by  $E_d/E_q$ ; where  $E_d$  is the mean exposure per pixel in the inner cell, and  $E_q$  is the same calculated for pixels in the outer cell but not the inner one.

The 21-pixel wide cell is not necessarily optimal. We therefore searched for any 21-pixel cell with an  $\text{SNR} \geq 1$ , and then investigated such cells further, by creating a  $17 \times 17$  pixel cell and stepping this around within the original 21-pixel cell (using an outer cell reduced in proportion). If one of these smaller cells had an SNR larger than was found in the 21-pixel cell, then its position and size were noted. The cell was then reduced to 15 pixels and stepped around inside the 21-pixel parent cell as before. This continued for cells of size 11, 9 and 7 pixels, with the cell always being moved in steps of  $d/3$  pixels ( $d$  is the width of the cell, the step size is rounded when non-integer) until no cell with an SNR greater than that in the 21-pixel region was found. Then all of the cells which were noted during this process were compared. If any cells overlapped, only that with the highest SNR was kept. For each cell thus found, a barycenter was calculated (using only counts within that cell), and also the box size with the maximal SNR was determined. If this box had  $\text{SNR} \geq 10$  then it was saved as an ‘excess’: a possible source.

Once the entire image had been searched in this way, any duplicate excesses were removed. If there were overlapping excesses<sup>7</sup>, the mean box size and position is determined, weighted according to the number of events in each cell. A barycenter was then calculated, and the overlap check repeated; this time where excesses overlap, only that with the highest SNR was kept; the others were discarded. The final result of this process was a unique list of excesses with  $\text{SNR} \geq 10$ .

### 3.3.2. Creating a background map

The above method assumes that there is at most a single source within the test cell; where multiple sources are close together this will therefore incorrectly estimate the background level. It also assumes that the cell is large enough to accurately sample the background and that this is invariant across the cell. These statements may be untrue.

We therefore produced background maps to accurately model the background across the detector and included in this map the sources which had already been detected. This process was repeated many times during the source

detection process and it is pivotal to our method: in Section 6.1 we demonstrate that it is reliable.

Even within a single observation, each snapshot covers a slightly different area of sky because it follows a new slew to the target. If we created a background map based on the full exposure, this would contain artifacts at the edges of the per-snapshot fields of view (particularly if the background level varies between snapshots, for example due to thermal variations in the passively-cooled XRT, Kennea et al. 2005). We therefore constructed the background map separately for each snapshot using the images and exposure maps created in Section 3.2, and then summed these to create the per-image background map. The process, described below, makes a single-snapshot, single-band background map, and was performed for each energy band and snapshot independently.

The first step was to create a detector mask. Initially all pixels in the mask were set to 1, then all pixels in the region of the excesses already identified were set to 0. The definition of ‘in the region of’ depended on the details of the excess. For all but the first and last background maps created for a dataset, the list of excesses comprised a mixture of those returned by the most recent cell detect run and those which had been PSF-fitted. For the former, the position and count rate were not well known, so the masking was approximate: the count rate of the excess was estimated based on the size of the cell in which the excess was detected and the standard XRT PSF, and pixels were masked out to the radius at which the count-rate dropped below  $10^{-5}$  ct sec<sup>-1</sup> pixel<sup>-1</sup> (or a maximum radius of 150 pixels). For PSF-fitted excesses the best-fitting PSF profile and count rate were known, so the mask radius was that where the count rate fell to  $10^{-6}$  ct sec<sup>-1</sup> pixel<sup>-1</sup> (a typical background level for an XRT exposure), again with a maximum of 150 pixels. If this process resulted in more than 80% of the image being masked out, the mask radius was reduced by 5% and the process reperformed; this was repeated until less than 80% of the image was masked (we set a maximum of 100 iterations, but this was never reached).

The mask was multiplied by the original image to create a masked image (referred to as a ‘Swiss-Cheese image’ by *Rosat* and *XMM*; Voges et al. 1999; Watson et al. 2009), i.e. one where ideally all events from the detected sources have been removed. This image was divided by the exposure map<sup>8</sup> and rebinned into a  $3 \times 3$  grid, with the uncertainty in each bin also calculated according to equation (1). If a box contained no unmasked pixels, the value of that box was set by interpolation from the neighboring boxes. The central pixel of each box was set to the value determined for that box, and the rest of the image was populated using bilinear interpolation from these nine values. The resultant image was then multiplied by the exposure map to give the background map. This process differs from the XMM approach of using spline interpolation over a finer grid than employed here, however that process tended to overfit the *Swift* background. The above approach of linear interpolation and a  $3 \times 3$  grid was arrived at through an extensive period of testing, and represents an excellent level of accuracy (Section 6.1) for a modest number of parameters.

<sup>7</sup> Because the 21-pixel cells are moved in steps of 7 pixels and thus overlap.

<sup>8</sup> Pixels with zero exposure are set to zero.

The uncertainties were propagated through this process to give a background error map.

Once the background had been modeled in this way, any excesses which had been PSF-fitted in previous iterations were added to the background (and background error) map; to reduce the number of spurious detections near to bright sources, and increase sensitivity to sources which are close together. This was done using the PSF profile from the PSF fit (Section 3.3.4) which has been modified to include the spokes caused by the shadow of the mirror support structure, and out-of-time events (see the Appendix).

The creation of a background map is illustrated in Fig. 4.

### 3.3.3. Sliding-cell detection using the background map

This process was almost identical to that described in Section 3.3.1, except that the outer cell was not used. Instead the background level,  $B$  was simply the sum of the background map within the cell, and hence

$$\text{SNR} = \frac{S}{\sigma_S} = \left( \frac{C - B}{\sqrt{\sigma_C^2 + \sigma_B^2}} \right) \quad (6)$$

where  $\sigma_C$  was defined as in Equation (1) and  $\sigma_B$  was taken from the background error map.

### 3.3.4. Source characterization using a PSF fit

The positions of the excesses were determined using a PSF fit based on that described in Goad et al. (2007) and Evans et al. (2009). A circular region was selected, centered on the position determined by the sliding-cell detection, with a radius based on the SNR of the excess as given in Table 3. The best position of the source was then determined by minimizing the C-stat (Cash 1979) as modified for use in XSPEC

$$\mathcal{C} = 2 \sum_i (M_i - D_i + D_i [\ln D_i - \ln M_i]) \quad (7)$$

where the sum is over all pixels in the circular region,  $D_i$  is the number of events measured in a pixel  $i$ , and  $M_i$  is the expected number of events in that pixel:

$$M_i = E_i (NP_i + B_i) \quad (8)$$

where  $E_i$  is the exposure,  $N$  is the normalization,  $P_i$  is the model PSF and  $B$  the value of the background map, in pixel  $i$ . We fitted for source position and normalization, using both the nominal PSF in the CALDB (Moretti et al. 2007) and the PSFs determined for piled-up sources (Evans et al. 2009); these were first modified to include the shadows of the telescope's mirror support structure (see Appendix A for details). Based on simulations, we required that  $\mathcal{C}$  decrease by at least 10 before accepting a more-piled-up PSF as a better fit. Although the PSF is a function of both energy and off-axis angle, the dependence on these factors is very small and we used the on-axis 1.5 keV profile for all of our fits. The 68% confidence intervals on the RA and declination were determined independently, by finding for each parameter the range of values within  $\Delta\mathcal{C} = 1$  of the best fitting  $\mathcal{C}$  value. This was later converted to a

**Table 3**  
The radius of the region used to perform PSF fitting.

SNR	Radius <sup>1</sup>
SNR $\leq 7$	12 pixels
7 < SNR $\leq 11$	15 pixels
11 < SNR $\leq 40$	20 pixels
SNR > 40	30 pixels
<b>Note.</b>	— 1
pixel=2.357''	

90% confidence radial error via Rayleigh statistics, using  $\sigma_{\text{Rayleigh}} = 0.5 * (\sigma_x + \sigma_y)$ . For a small number of objects, the fit was unable to determine the uncertainty due to minimization errors. In these cases we set the 90% confidence radial error to be  $14.6''/\sqrt{N}$  (where  $N$  is the number of events in the fitting region), this relationship having been calibrated from simulations.

We then reconstructed the count-rate of the source, needed for the background map. For most sources this was done using a circular region with radius as for the PSF fit, but centered on the position returned by that fit. However if the best-fitting PSF was one of the piled-up profiles, or if the estimated count-rate in the original circle was  $>0.6 \text{ ct s}^{-1}$  (the level at which pile-up tends to become significant) an annular region was instead used, with the inner radius given in Table 4; these reflect the radii at which the piled-up PSFs become asymptotic to the non-piled-up PSF. The outer radius was still that used for the PSF fit if this was larger than the inner radius, otherwise it was 5 pixels more than that value.

The measured and background counts,  $C$  and  $B$ , were taken from the image and background map respectively in the region just defined. If  $(C - B) > 30$  then the estimated number of source events,  $S = C - B \pm \sqrt{C + B}$  as in Equation 6 (except that we define  $\sigma_C = \sqrt{C}$  as we are no longer in the low-count regime). For lower numbers of measured counts the value  $S$  was determined using the Bayesian method of Kraft et al. (1991)<sup>9</sup>. To correct for the effects of pileup, vignetting and exposure variations (e.g. due to dead columns on the CCD) we calculated the correction factor:

$$\kappa = P_{\text{inf}}/P_{\text{meas}} \quad (9)$$

where

$$P_{\text{inf}} = \sum_{i, r=150} (E_{im} P_i) \quad (10)$$

$$P_{\text{meas}} = \sum_i (E_i P_i) \quad (11)$$

$P_{\text{inf}}$  is the PSF summed from a radius of 0 out to 150 pixels (effectively infinity), while  $P_{\text{meas}}$  was summed only over the region from which counts were measured.  $E_{im}$  is

<sup>9</sup> At  $C - B = 30$  the Bayesian calculation converges with the standard approach. However, the Bayesian approach assumes that there is no uncertainty in the background measurement which in principle leads to an underestimate of the error. For typical detections in our catalog this is at the 0.1% level, so can be ignored.

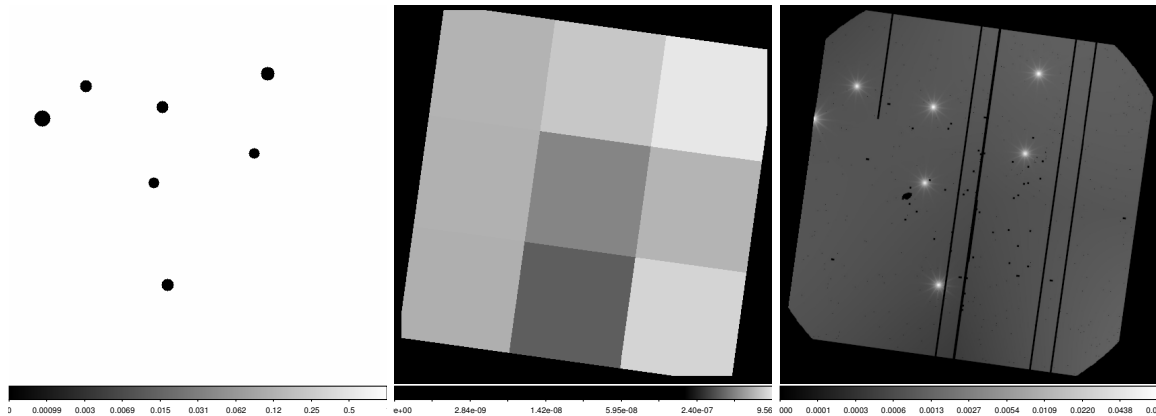


**Figure 4.** Example stages of background map creation on a single snapshot. *Left:* The detector mask; white pixels are ‘on’ while black ones are masked out. *Center:* The rebinned background. *Right:* The final background map, including the model PSFs of the sources detected so far.

**Table 4**

The inner radius of the annular region used to measure the count-rate for piled up sources.

Fitted PSF profile	Radius
CALDB	3 pixels
rate=0.9 ct s <sup>-1</sup>	4 pixels
rate=1.4 ct s <sup>-1</sup>	6 pixels
rate=2.6 ct s <sup>-1</sup>	7 pixels
rate=4.0 ct s <sup>-1</sup>	8 pixels
rate=5.2 ct s <sup>-1</sup>	13 pixels
rate=8.6 ct s <sup>-1</sup>	20 pixels
rate=15 ct s <sup>-1</sup>	25 pixels

**Note.** — The ‘CALDB’ profile is that determined by Moretti et al. (2007) and given in the CALDB. The remainder were determined by Evans et al. (2009). The ‘rate’ is related to the object used to calibrate the PSF and not to the source being characterized in this catalog. The PSF profile used to determine the count-rate correction factor is the one determined in the PSF fitting stage.

the on-axis exposure of the image. The estimated source count-rate is thus:

$$R = \frac{\kappa S}{E_{im}} \quad (12)$$

We next checked for potential duplicates or detections of the same astrophysical object. These can occur in the PSF wings and diffraction spikes of bright sources, even though these were added to the background map at each iteration. We therefore checked the distance of each newly-fitted excess from those found in previous iterations. If it lay within the distance tabulated in Table 5 it was assumed to be an alias of that object, and was discarded. This means that our detection method is blind to new sources in the close vicinity of brighter objects, however the tendency to detect false positives in this region had effectively blinded the system anyway. Due to the nature of *Swift*’s observing strategy, this limit is often only temporary. For example, a newly detected GRB

**Table 5**

The distance from a source within which detections are assumed to be artifacts.

Source rate (count/sec)	Radius (pixels)
$R \leq 0.4$	10
$0.5 < R \leq 1$	35
$1 < R \leq 2$	40
$2 < R \leq 8$	47
$R > 8$	70

is usually bright, so the radius over which we cannot detect new sources is large, however the GRB is observed again as it fades; in those later observations sources close to the GRB can be reliably detected.

### 3.3.5. Detection likelihood

After PSF-fitting an excess we calculated  $\mathcal{C}$  a second time with the normalization set to 0, i.e. with no source present. Since  $\Delta\mathcal{C}$  is distributed as  $\Delta\chi^2$  (Cash 1979; here with two degrees of freedom,  $\nu = 2$ ) we determined the probability that the change in fit statistic with and without a source present is coincidence:  $P = \Gamma(\nu/2, \Delta\mathcal{C}/2)$  (where  $\Gamma$  is the incomplete Gamma function), and the log-likelihood,  $L = -\ln(P)$ . As Watson et al. (2009) pointed out, we cannot take this statistic at face value; indeed the false positive levels they report are 10–100 times higher than expected from the equations above for the likelihood values they quote. This is because the measurement with no source present is a boundary condition of the model: as the source normalization cannot be negative, the test with normalization set to 0 is at the limit of the allowable model space. In such cases the likelihood ratio does not follow a  $\chi^2$  distribution (see Prottassov et al. 2002 for a detailed discussion). Like Watson et al. (2009) we instead calibrated the relationship between  $L$  and  $P_{\text{false}}$  using simulations, as described in the Section 6. Based on this calibration, we rejected any excess with  $L < 3$ .

### 3.4. Quality flags and further checks

Several further tests were performed to eliminate spurious or extended sources and to indicate how reliable



a given detection is. Spurious detections can arise due to hot columns and hot rows on the detector. For each excess, we selected from the relevant event list all the events lying within the PSF fitted region. Only excesses containing events from at least three distinct detector pixels, rows and columns were accepted; in addition, any excess where  $>50\%$  of the events lie in a single pixel, or  $>75\%$  lie within a single row or column was discarded. After this the location of each surviving excess was compared to a list of known extended objects (taken from Tundo et al. 2012): if the excess lay within the extent of the extended object it was discarded.

The remaining excesses are considered to be detections of genuine astrophysical sources, but some level of contamination will remain: we therefore assigned each source a quality flag to indicate the probability that it is a false positive. This flag is a function of the exposure time and the likelihood value for the source, and can be either *Good*, *Reasonable* or *Poor* (with corresponding integer values of 0, 1 and 2). If only *Good* sources are considered, the false positive rate is 0.3%; if *Good* and *Reasonable* sources are included, this rises to 1%, and if *Poor* sources are also considered, the false positive rate is 10%. Of course the fraction of true sources that are detected (i.e. the completeness) also rises as *Reasonable* and *Poor* detections are included. This allows users to easily choose between sample size and sample purity. Full details of the definitions of the quality flags and how the false positive rate and completeness fraction were calibrated are given in Section 7.

There is an additional category of sources, *Bad*, which is not included in our catalog. Such sources were accepted by the source detection code, but as they have a very high false positive rate ( $\sim 80\%$ ) they were rejected before the detections are merged (Section 3.5). The background map was reconstructed at this point without the *Bad* detections considered. This new background map was used for construction of the source count rates and light curves. We stored a list of these *Bad* detections for use with the upper limit server (Section 4.4).

We also performed an automated check for the phenomenon called *optical loading*. Bright optical sources can liberate sufficient charge in the XRT CCD because of the large number of optical photons accumulated in a 2.5-s PC mode exposure frame that the characteristics of X-ray events at the location of the optical source are distorted. When this first becomes a problem, it causes the energy of the X-ray events to be overestimated<sup>10</sup>. At higher optical fluxes, it can cause real X-ray events to be discarded or spurious events to be detected. The flux at which this occurs is a function of stellar color and is discussed in detail at [http://www.swift.ac.uk/analysis/xrt/optical\\_loading.php](http://www.swift.ac.uk/analysis/xrt/optical_loading.php); stars brighter than  $V \sim 9$  can be a problem, the limit being more severe for those later than  $M0$ . We set a threshold at which optical loading is to be flagged as that at which a star contributes spurious events at a level of  $\geq 10^{-3}$  ct s<sup>-1</sup>. We searched for cataloged stars above this threshold within  $30''$  of each X-ray source in our catalog, using their cataloged  $B - V$  color to estimate spectral type and hence determine the

$V$  magnitude limit. If such a star was found, a field OL\_WARN is set in the catalog, indicating how many magnitudes brighter than the threshold the star is. We used the Tycho-2 (Høg et al. 2000), Bright Star Catalog (Warren & Hoffleit 1987) and General Catalog Of Variable Stars (Samus et al. 2010) as our source of optical objects. These sometimes contain the peak magnitude of a variable object, which may not be appropriate to the *Swift* observations (e.g. GK Perseii has a catalog magnitude of  $\sim 0$ , based on its nova eruption of 1908; but was at least 10 magnitudes fainter during all *Swift* observations), so a large OL\_WARN value should be taken as a warning that an object *may* be affected by optical loading, rather than that it is affected.

### 3.5. Merging detections across bands

Since the detection system was performed independently on the four energy bands within a dataset, the list of sources detected in each band had to be merged to create a unique list of sources for that dataset. This was done by considering the detected sources in descending order of SNR and then using the radii given in Table 5 to determine which detections correspond to the same object. Where a source was detected in multiple energy bands, the definitive position of that source (in this dataset) was taken from the detection with the smallest position error (provided this is not one where the error could not be determined from the fit).

For a source which was undetected in one or more energy bands, the images of those bands were examined to determine the number of events at the source location. The expected background level was determined from the corresponding background map. The count-rate and error for this energy band was then estimated using the Bayesian approach of Kraft et al. (1991) and the PSF correction  $\kappa$  was applied as for detected sources. Although the source was undetected in this case, we did not produce an upper limit, even though the count-rate may well be consistent with zero. Instead we determined the value and the 68% (i.e.  $1-\sigma$ ) confidence limits, as we do for detections. Note that we give the positive and negative uncertainties separately as, when using the Bayesian approach, they may not be the same.

We also determined two hardness ratios, defined as

$$\text{HR1} = (M - S)/(M + S) \quad (13)$$

$$\text{HR2} = (H - M)/(H + M) \quad (14)$$

Where  $S, M, H$  refer to the soft, medium and hard bands respectively. If both bands in the hardness ratio contained  $> 100$  counts, and had a  $\text{SNR} > 2$  then the ratios were calculated using the above equations, with the errors on  $H, S$  and  $M$  taken as  $\sqrt{\{H, M, S\}}$  respectively and propagated through equations 13 and 14. For fainter sources we used the Bayesian method of Park et al. (2006), where we used the effective area option in their code to include the count-rate correction factors in the calculation. While the Bayesian method gives asymmetric errors (which are typically a few percent larger than the standard method returns), the standard method returns symmetric errors. This means one can find, for example,  $\text{HR1} = 0.95 \pm 0.1$ , even though the HR must be

<sup>10</sup> A correction for this is made by the XRTGCCORR tool called by XRTPIPELINE as part of the standard processing.

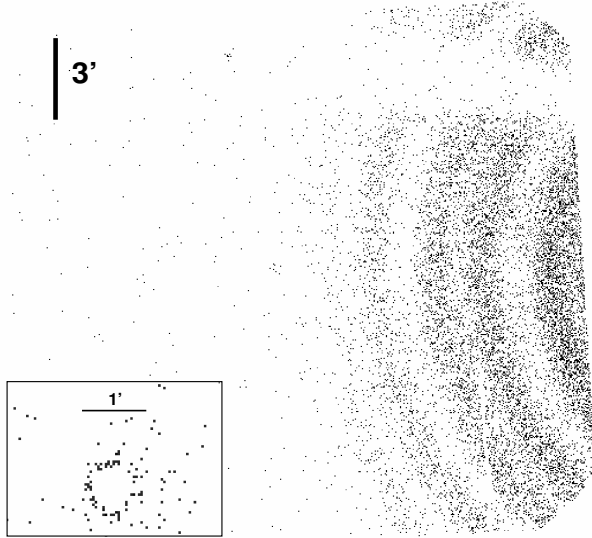


**Figure 5.** Examples of artifacts that were identified by manual screening. The main plot shows *stray light*: caused by single reflections from a bright source lying outside the XRT field of view – in this case the Crab nebula, lying 45’ off-axis. The gap in the rings is the shadow of the mirror support structure. *Inset*: a ‘ring of fire’: the apparent X-ray events were caused by accumulation of optical photons from a bright star (a  $V = 3$  Be star in this example). Towards the center of the star’s location no events are detected because the optical flux is so high that in a single 2.5-s CCD exposure frame all pixels register events, and thus the event ‘grade’ (which describes how many pixels a given event affected) is above the maximum value permitted for valid events.

between  $-1$  and  $1$  (inclusive). In such cases of course, the true HR limit is  $+1$  (or  $-1$  in a negative counterexample).

### 3.6. Manual screening

While the quality flagging system based on the source likelihood values is reliable for celestial point sources, it can be deceived in the presence of structured diffuse emission (e.g. from a supernova remnant) or instrumental artifacts. The most common of these artifacts is *stray light* (Moretti et al. 2009): X-ray photons from a source 35’–75’ off-axis (i.e. outside the field of view) that are directed onto the XRT detector via a single reflection (as opposed to the double reflection which focuses X-rays). This occurs at a very low level: the effective area of the XRT for a source 50’ off-axis is  $\sim 33,000$  times lower than that on axis, and the singly-reflected photons are distributed over a much wider area of the CCD than for a focused source. Nonetheless, sufficiently bright sources outside the field of view can cause concentric arcs of events to be detected in the CCD (Fig. 5) which can give rise to spurious source detections.

The typical background level of the observations in our catalog is  $\sim 10^{-6}$  ct sec $^{-1}$  pixel $^{-1}$ ; for a source outside the field of view to contribute stray light at this level it would require an on-axis XRT count-rate of  $\sim 3$  ct sec $^{-1}$ . We conservatively chose a limit of 1 ct sec $^{-1}$ , which corresponds to a 0.3–10 keV flux of  $3.5 \times 10^{-11}$  erg cm $^{-2}$ s $^{-1}$  assuming a typical AGN spectrum: a power-law spectrum with  $N_H = 3 \times 10^{20}$  cm $^{-2}$  and  $\Gamma = 1.7$ . We identified all sources in the *Rosat* PSPC and 2XMMiDR3 catalogs with fluxes above this limit, and selected for manual screening all fields in our catalog that lay

within 28’–82’ of those sources. This did not identify all fields affected by stray light, as 2XMMiDR3 covers only a small fraction of the sky, *Rosat* is not sensitive to strongly absorbed or hard sources and some objects are variable.

There are other artifacts that can contaminate the images. These are residual bright Earth contamination, the ‘ring of fire’ effect caused by serious optical loading (Fig. 5, bottom) and the presence of extended sources or diffuse emission. All of these effects (and stray light) give rise to spatially proximate spurious detections. For this reason we also selected for manual screening any image where the median distance between detections was  $< 80''$ . In total 15,152 datasets (out of 56,275 in the catalog) were selected for human inspection.

We inspected these images in decreasing order of exposure time. If an image was deemed to be affected by the artifacts described above, then the results of this screening was applied to all pointings covering that location on the sky, avoiding the need to check each image individually. When artifacts were manually identified, regions were defined which encompassed them, and any sources which lay within those regions had their detection flags changed. The ‘Field flag’ for the image was also set from its default value of *Good* ( $=0$ ) to *Flagged* ( $=1$  or  $2$ ). For images containing artifacts (stray light, bright Earth or rings of fire) the detection flag of affected sources was increased (from 0, 1 or 2) by 8 and the field flag set to 1. For images containing diffuse emission the detection flag of affected sources was increased by 16 and the field flag set to 2.

We distinguish between artifacts and diffuse emission because, while both of these phenomena affect the background map (by causing inhomogeneities over which the background map attempts to smooth and interpolate, and potentially by causing the detection of spurious sources which in turn are added into the background map), artifacts have well defined edges, but it is often not clear where a diffuse source stops contributing to the background. For this reason (given that a dataset can only have a single field flag value) where both artifacts and diffuse emission were identified in an image, the flag was set for the latter.

The result of the screening is that any source with a detection flag with a value  $\geq 8$  (i.e. lying inside a *region* which has been manually marked as contaminated) has a high probability of being spurious, whereas sources with a flag value below this but lying in a *Flagged* field (i.e. in the field, but outside the region manually marked as bad) have false positive rates as described in Section 3.4, but may have incorrect background values and thus measured source fluxes.

### 3.7. Astrometric corrections

We attempted to derive a more accurate astrometric solution for our datasets than that available from the star trackers mounted on the XRT. The latter gives positions accurate to 3.5’’ 90% of the time (Moretti et al. 2007). For each dataset, we matched the *Good* and *Reasonable* sources with the 2MASS catalog (Skrutskie et al. 2006) using an approach similar to that employed by Butler (2007). For every dataset in which more than two X-ray sources were detected, we retrieved a list of 2MASS objects that lay within the XRT field of view and attempted

to find an aspect solution for the field which maximized the likelihood:

$$L = \sum_{\text{ox} < 20} e^{(-0.5\delta^2/\sigma^2)} \quad (15)$$

where  $\text{ox}$  is the angular separation between each *Good* and *Reasonable* XRT source and each 2MASS source, so the sum is over all XRT/2MASS source pairs within  $20''$  of each other;  $\delta$  is the angular distance between the 2MASS and XRT sources in question, and  $\sigma$  is the radial uncertainty in the two positions added in quadrature. The  $1\text{-}\sigma$  uncertainty in the aspect solution thus derived was taken as the RMS of the  $\delta$  value for each 2MASS/XRT pair in the final fit. If the mean shift in any of the X-ray positions as a result of this process was  $> 15''$  then the solution was considered unreliable and rejected: this distance corresponds to a  $7\text{-}\sigma$  inaccuracy in the star tracker solution, which is a most unlikely situation.

This process could not find an astrometric solution for every dataset, and in the majority of cases where a solution was found, the uncertainty in the aspect solution was  $> 3.5''$ ; in these cases we used the star tracker attitude. A solution with an error  $< 3.5''$  was found for only 4% of the datasets in our catalog, but as these were the datasets with objects in them, 26% of the sources in our final catalog have positions improved using this technique. Whichever method was used, the astrometric error was added in quadrature to the statistical position error from the PSF fit (Section 3.3.4) to give the radial position error reported in the catalog.

To verify that this method gives reliable positions and uncertainties, we applied it to the fields containing the 999 objects in our catalog which are within  $20''$  of quasars in the SDSS Quasar Catalog DR5 (Schneider et al. 2007) and thus likely to be the X-ray counterpart to the quasar. We found that 90% of the XRT positions thus produced agreed with the SDSS positions at the 90% confidence level, as expected.

### 3.8. Building the final unique source list

Once the above steps had been completed for every dataset contributing to the catalog, we merged the lists of sources from each dataset into one final source list. This was done in the same way as described in Section 3.5, except that instead of using fixed merge radii based on the source brightness, different detections were assumed to be the same source if their positions agreed at the 99.99999426% level<sup>11</sup>. For a typical source this was  $\sim 14''$  ( $\sim 6$  XRT pixels), which is 75% of the PSF FWHM and the probability of distinct sources lying this close to each other is very low,  $\ll 1\%$ .

This approach takes into account the fact that different observations may have different astrometric accuracy, and allows for faint sources that are near to a bright source, but not detected until after that object has faded, to be distinguished from the bright source.

<sup>11</sup> i.e. the  $5\text{-}\sigma$  level of a Gaussian distribution. Since radial errors follow a Rayleigh distribution, we use the probability level, not the number of  $\sigma$ . By ‘the positions agreed’ at this level we mean that the probability from Rayleigh statistics of their separation being that observed or lower, given their position errors, is less than this threshold.

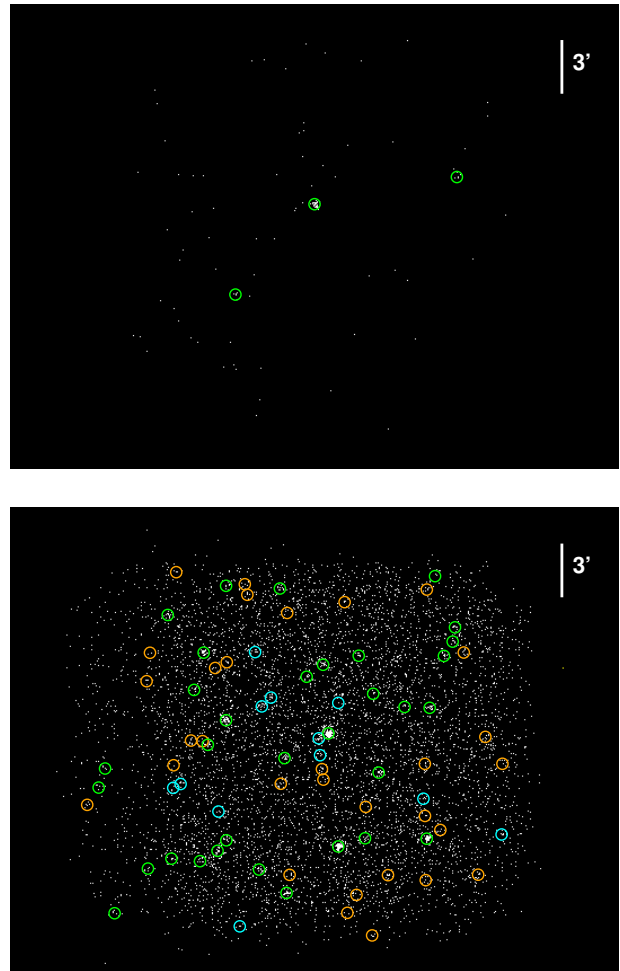


**Figure 6.** Example datasets from the catalog. Both images are from the total band (0.3–10 keV) with pixel intensity following a log scale. *Top*: a short single observation, (ObsID 00032165001, exposure 424 s) with the three sources detected in that observation and band shown. *Bottom*: a deep stacked image (field 7086, exposure 1.1 Ms); the final unique source list for this region is shown. The regions indicate objects detected, with the ‘quality’ of the detection shown by the color: green=*Good*, cyan=*Reasonable*, orange=*Poor*. The regions are a fixed size and do not reflect the size of the region used in source detection.

When compiling this final source list, the detection flag in each band was set to the best of the detection flags in that band from the individual detections of the source. A final, overall detection flag was also produced which was the best of the per-band flags, and likewise for the field flag. The optical loading warning was set to be the worst value from the set of individual detections of the source. The final source position was taken from the detection with the smallest position error, and the source was given a unique designation of the form: 1SXPS JHH-MMSS.S+DDMMSS. This acronym has been registered with the IAU.

Fig. 6 shows two examples of datasets after all of the steps in this section have been applied.

## 4. SOURCE-SPECIFIC PRODUCTS

The details of the unique sources and the individual detections are available in the form of catalog tables, available to query online or and download (Section 5). In addition to these, we have produced light curves, hardness

ratios and variability and flux estimates for each source, and spectra for the brightest sources, as described below. These products are available to download via the 1SXPS website, where tools also exist to calculate upper limits for specific locations on the sky.

#### 4.1. Temporal products

We produced light curves in each of the four energy bands, with one bin per observation and one bin per snapshot (for observations where the source is undetected the latter light curve only contains a single bin integrated over that observation). We also produced time series of the hardness ratios with one bin per observation. The times of each bin in all of these products were corrected to the solar system barycenter (i.e. TDB).

To construct the time series, the count rate in each snapshot or observation was determined as described in Section 3.3.4, except that we used the best source position determined per observation (see Section 3.5), to account for the potential differences in astrometry between observations. The source-count accumulation region used was also that from Section 3.5 if the source was detected; for bands, snapshots or observations where the source was not detected a circular region of radius 12 pixels ( $28.3''$ ) was used.

For the time series in each band we calculated used the Pearson's  $\chi^2$  (Pearson 1900) to determine the probability that the source was variable. The Pearson's  $\chi^2$  is defined as:

$$\chi^2 = \sum_i \left\{ \frac{(D_i - M_i)^2}{M_i} \right\} \quad (16)$$

where  $D$  and  $M$  are the data and model in bin  $i$  respectively. These must be not in units of the count-rate (as contained in the light curve), but the measured number of counts ( $C$ ) in each bin. Since we test for the null hypothesis that the source is constant, the model is that of constant source flux, but this is not the same as constant source counts in each bin as the exposure time ( $E$ ) and count-rate correction factor ( $\kappa$ , see Section 3.3.4) can vary from bin to bin. Explicitly including these factors and the background level, if the source is constant the count rate is the same in each bin and is simply the mean value; which can be determined from the measurements thus:

$$\begin{aligned} R_i &= \text{const} \\ &= \frac{(C_i - B_i)\kappa_i}{E_i} \\ &= \frac{\sum_j \{\kappa_j (C_j - B_j)\}}{E_{\text{tot}}} \end{aligned} \quad (17)$$

where the summation is over all bins, and gives the total number of PSF-corrected counts over the light curve. We can then solve the above to determine the model of the number of counts per bin:

$$\begin{aligned} M_i &= C_i \\ &= \left( \frac{E_i}{E_{\text{tot}}} \right) \left( \frac{\sum_j \{\kappa_j (C_j - B_j)\}}{\kappa_i} \right) + B_i \end{aligned} \quad (18)$$

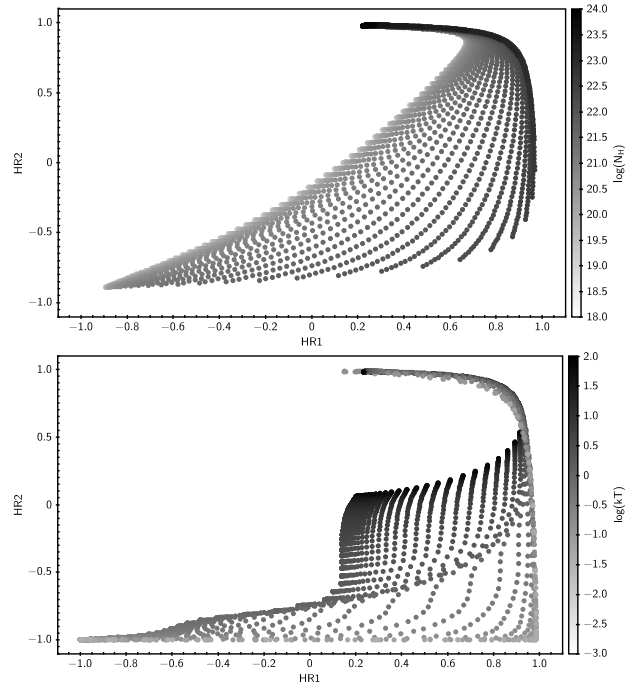


**Figure 7.** The (HR1,HR2) plots used to deduce spectral information for the sources. *Top:* For a power-law spectrum, the  $N_H$  values (grayscale) as a function of (HR1,HR2); each point also has a  $\Gamma$  value and ECF, not shown here. *Bottom:* For an APEC spectrum, the  $kT$  values are shown as the grayscale. Each point also has  $N_H$  and ECF values not shown here.

This test, which reports the probability of the null hypothesis that the source is constant, was applied to both the per-snapshot and per-observation light curves (but not the hardness ratio time series), probing variability on multiple timescales. To ensure that the per-snapshot result is not affected by variation on the per-observation timescale, we calculated  $\chi^2$  and hence  $P$  for the per-snapshot light curve of each observation independently, and then report the lowest value thus obtained.

We also tried using the Wald-Wolfowitz runs test (Wald & Wolfowitz 1940) as an independent measure of variability, however this lacked the power to identify variable sources in our catalog, probably because many light curves have small numbers of bins. We therefore elected not to include these results in the catalog.

#### 4.2. Flux conversions and spectra.

For every source in the catalog we created energy conversion factors (ECF) to convert from count-rate to flux (observed and unabsorbed)<sup>12</sup> We did this for two commonly observed spectral types: an absorbed power-law and an absorbed APEC optically thin thermal plasma model (Smith et al. 2001); for the latter we assumed solar abundances. The absorption was modeled using the TBABS model (Wilms et al. 2000).

For each source in the catalog we first determined ECFs using standardized spectra: a power-law with a photon index of 1.7, and an APEC with a temperature of 1 keV; the absorption was fixed at the Galactic value in

<sup>12</sup> The uncertainty in the ECF was not propagated into the error on the flux; this was simply the count-rate error multiplied by the ECF.

the direction of the source, determined using the NHTOT tool of Willingale et al. (2013).

We also estimated the flux and spectral parameters from the hardness ratio information. Using XSPEC we simulated a series of spectra, with  $17 \leq \log N_H / (1 \text{ cm}^{-2}) \leq 24$ ; for the power-law spectrum we used photon indices in the range  $-3 \leq \Gamma \leq 5$  and for the APEC spectrum we used temperatures  $-2 \leq \log(kT/1\text{keV}) \leq 1.9$ . We folded each simulated spectrum through the instrument response to derive its ECF and its two hardness ratios. We used the latter to construct a look-up table of the spectral parameters as a function of (HR1, HR2); examples are given in Fig. 7. For each source in our catalog, if (HR1,HR2) lay in the region covered by the simulated spectra we interpolated on this grid to ascertain the spectral parameters of the source. We also did this for the four points given by  $(\text{HR1} \pm \sigma_{\text{HR1}}, \text{HR2} \pm \sigma_{\text{HR2}})$  to estimate the uncertainty on these properties. For any of those limits which lay outside the range covered by the simulated spectra, we took the values for the (HR1,HR2) point nearest to the limit in question. Note that the range of parameters for the simulated spectra goes beyond what we may physically expect for XRT sources, in such extreme cases the purpose of this approach is to give reasonable flux estimates within the 0.3–10 keV band, over which the model gives an acceptable approximation to the data. However the actual the spectral parameters themselves should be viewed with caution in those cases, and care should be used before extrapolating outside of the XRT bandpass.

For sources where (HR1, HR2) lay outside the range covered by the simulated spectra we cannot calculate the spectral parameters in this way, instead we determined the probability of measuring (HR1,HR2) if the true spectrum were that of the simulated spectrum with hardness ratios closest to the measured values, given the uncertainties on those values.

For the sources with at least 50 net events in the total band, we also built spectra using the software of Evans et al. (2009). We fitted these with an absorbed power-law and absorbed APEC, with all parameters unconstrained (i.e. the fitted absorption was independent of the expected Galactic value). The fit was performed on spectra binned to at least one photon per bin (i.e. GROUP MIN 1 in GRPPHA), fitted using the XSPEC *W*-statistic<sup>13</sup>; after fitting we calculated  $\chi^2$  using the Churazov weighting option (Churazov et al. 1996) to indicate the fit quality and allow users to reject poor fits. Note that this is not a reliable goodness-of-fit indicator (see Churazov et al. 1996, section 3.2) and cannot be used to calculate the null hypothesis probability.

In the final catalog table we report the spectral properties derived through all three of the above methods (fixed spectra, interpolation of the HR values, and spectral fitting) where they are available. Since not all objects have all of the properties, this can make comparison of sources awkward, we have therefore included in the catalog a set of ‘best spectral properties’. These are taken from the spectral fit if it exists, otherwise the HR interpolation, and if neither of those is available, the results from the

fixed spectrum are used here.

#### 4.3. Cross correlation with external catalogs

We cross-correlated the 1SXPS catalog with various external catalogs and databases, defining a source match to be where the 1SXPS and external catalog positions agree at the 99.7% level<sup>14</sup>. SIMBAD<sup>15</sup> contains some sources from the facility-specific catalogs that we searched; such sources were only taken from the facility catalogs rather than repeating the match via SIMBAD/NED. We assumed zero position uncertainty for the SIMBAD, USNO-B1, 2MASS, NED and SDSS QSO catalogs, using just the 1SXPS position errors. For the USNO-B1, 2MASS and SDSS catalogs this is because their position errors are negligible compared to the 1SXPS errors. For SIMBAD and NED we are not able to specify the search radius as a function of source error in the remote query, and error information is not available in a uniform way; this may mean that for these catalogs the number of real matches which are not reported is higher than for the other catalogs. For the remaining catalogs we used the 1SXPS and catalog error added in quadrature. In some catalogs the systematic error is given only in the supporting documentation. This was added in quadrature to the catalog’s statistical error when available. Details of the catalogs and their systematic errors are given in Table 6, along with the number of 1SXPS sources which have a match in each catalog. Spatial coincidence alone of course does not guarantee association between the 1SXPS source and that in the external catalog. To estimate the number of spurious matches in this correlation, we shifted the position of each 1SXPS source at random by 1–2’ and repeated the correlation test. The number of matches found to these positions are also shown in Table 6.

Due to the high sky density of the 2MASS and USNO-B1 catalogs, the number of expected spurious matches is very high at > 50%. Indeed, there are frequently multiple matches from these catalogs to a single 1SXPS source, indicating that a 3- $\sigma$  spatial coincidence in this case it a poor indicator of association.

We therefore ignored matches from these catalogs to estimate the number of new sources in our catalog: we found 68,638 1SXPS objects which are uncataloged (i.e. had no external catalog matches) in this case. However, as Table 6 shows, despite these considerations there are 62,712 objects without a match in the USNO-B1 catalog and 99,353 without a match in the 2MASS source; in total there are 20,390 sources in the 1SXPS catalog with no counterpart in any of the catalogs against which we performed a cross-correlation.

#### 4.4. Upper limit server

The 1SXPS website includes an upper limit server, which allows upper limits to be calculated for any sky

<sup>14</sup> i.e. the Gaussian ‘3- $\sigma$ ’ level, although as we used Rayleigh statistics we did not use 3- $\sigma$ , but 99.7%. This is smaller than the search radius used to merge distinct 1SXPS detections in to a unique source list, because the sky density of some external catalogs is high, and the number of spurious associations expected using a ‘5- $\sigma$ ’ radius was unacceptably large

<sup>15</sup> The SIMBAD and NED catalogs are dynamic entities: we cross-correlated against SIMBAD on 2013 June 10 and NED on 2013 September 6.

<sup>13</sup> i.e. by requesting the *C*-statistic and then providing a background spectrum with Poisson statistics, see <https://heasarc.gsfc.nasa.gov/xanadu/xspec/manual/XSappendixStatistics.html>

**Table 6**  
Catalogs cross-correlated with 1SXPS.

Catalog	Systematic Error <sup>1</sup>	Number of matches <sup>2</sup>	Spurious matches <sup>3</sup>
SDSS Quasar Catalog DR5 <sup>4</sup>		1,781	9 (0.5%)
XRTGRB <sup>5</sup>		659	6 (1%)
SwiftFT <sup>6</sup>		9,154	268 (3%)
1SWXRT <sup>7</sup>		35,009	1,669 (5%)
1CSC <sup>8</sup>		6,334	340 (5%)
3XMM DR4 <sup>9</sup>		19,649	1,381 (7%)
ROSHRI <sup>10</sup>	10''	1,930	171 (9%)
SIMBAD <sup>11</sup>		17,708	2,000 (11%)
XMM SL1 <sup>12</sup>	17''	2,212	378 (17%)
ROSPSPC <sup>13</sup>	25''	4,968	1,082 (22%)
NED <sup>14</sup>		49,098	14,761 (30%)
USNO-B1 <sup>15</sup>		88,812	48,718 (55%)
2MASS <sup>16</sup>		52,171	33,549 (64%)

**Note.** — <sup>1</sup> 90% confidence

<sup>2</sup> Number of 1SXPS sources for which there is a counterpart in the external catalog within  $3\sigma$ .

<sup>3</sup> The number of 1SXPS sources with a match after the 1SXPS position has been moved by 1–2'; the value in brackets is this number as a percentage of the matches to 1SXPS positions for the same external catalog.

<sup>4</sup>Schneider et al. (2007); <sup>5</sup> Taken from [http://www.swift.ac.uk/xrt\\_positions](http://www.swift.ac.uk/xrt_positions); see Evans et al. (2009); <sup>6</sup> Puccetti et al. (2011); <sup>7</sup> D'Elia et al. (2013); <sup>8</sup> Evans et al. (2010); <sup>9</sup> <http://xmmssc-www.star.le.ac.uk/Catalogue/3XMM-DR4/>; <sup>10</sup> <http://heasarc.gsfc.nasa.gov/W3Browse/rosat/roshri.html> <sup>11</sup> <http://simbad.u-strasbg.fr/simbad/> <sup>12</sup> Saxton et al. (2008); <sup>13</sup> Voges et al. (1999); <sup>14</sup> <http://ned.ipac.caltech.edu/>; <sup>15</sup> Monet et al. (2003); <sup>16</sup> Skrutskie et al. (2006)

location covered by our catalog. If the location was observed in more than one observation, upper limits can be calculated per observation, or from the stacked image in which those observations are included. To calculate the upper limit a 12-pixel radius circle is placed on the image at the location in question, and the number of events in that circle is registered. The background level in this region is taken from the corresponding background map. Then the Bayesian method of Kraft et al. (1991) is used to determine the upper limit on the source count-rate at the confidence level specified by the user. If the location requested matches that of a *Bad* detection which was discarded from the catalog (Section 3.4), this is also reported.

## 5. CATALOG CHARACTERISTICS AND AVAILABILITY

The 1SXPS catalog contains 151,524 sources; 135,086 of which are not in flagged regions (Section 3.6). The median 90% confidence radial position error of the sources in the full catalog is  $5.5''$ , including systematic errors, and the median 0.3–10 keV flux is  $3 \times 10^{-14}$  erg cm<sup>-2</sup> s<sup>-1</sup>. The total exposure time of the observations in the catalog is 147 Ms, spread over 1905 square degrees on the sky. 10% of the exposure time lies at a Galactic latitude  $|b| < 3^\circ$ ; 14% of 1SXPS sources lie in this latitude range, showing as expected an overdensity of sources in the Galactic plane compared to the sky as a whole.

The catalog of sources and their properties is available

for download as a FITS or ASCII table from the 1SXPS website: <http://www.swift.ac.uk/1SXPS>. Table 7 describes the columns in the catalog. This website also provides simple and comprehensive search facilities, a detailed web page for each source and each dataset, as well as the upper limit server (Section 4.4). The main catalog file is also available through Vizier (catalog ID: IX/43).

A table of external catalog cross correlations (Section 4.3) is available from the site above, as are tables giving information about the individual detections and the datasets. These tables are described in Tables 8–10. We request that publications which make use of this catalog state in the acknowledgements: *This work made use of data supplied by the UK Swift Science Data Centre at the University of Leicester.* as well as citing this paper.

When selecting objects from the tables, the combination of detection flags and field flags gives great control over whether sensitivity or purity is prioritized. The catalog website also provides postage-stamp images of each source and images of each dataset; when considering sources with detection flags  $\geq 8$  it is recommended to view these images to help judge their reliability. For the rest of this paper we conservatively defined a ‘clean’ subsample of the catalog, comprising all objects with detection and field flags both  $< 2$  (i.e. *Good* or *Reasonable*, and from a field that is either OK, or affected only by artifacts but not in the region covered by the artifact): there are 98,762 such sources in the catalog.

**Table 7**  
Contents of the main catalog table (‘sources’)

Field	Units	Description	Has errors? <sup>1</sup>
<i>Name and position</i>			
Name	Unique identifier, of the form: 1SXPS JHHMMSS.S+DDMMSS		

Table 7 — *Continued*

Field	Units	Description	Has errors? <sup>1</sup>
RA	degrees	Right Ascension (J2000)	
Decl	degrees	Declination (J2000)	
Err90	arcsec	90% conf. radial position error	
AstromType		The provenance of the astrometry used for the source position. 0= <i>Swift</i> star tracker, 1=XRT/2MASS correlation	
l	degrees	Galactic longitude	
b	degrees	Galactic latitude	
OffAxis	arcmin	The mean off-axis angle of this source from the observations in which it was detected	
		<i>Exposure details</i>	
Exposure	s	The total exposure at the source location	
StartDate	UT	The calendar date of the start of the first observation of the location of this source	
StopDate	UT	The calendar date of the end of the last observation of the location of this source	
NumObs		The number of observations of the location of the source	
NumDetObs		The number of observations in which the source was detected	
		<i>Flag details</i>	
DetFlag		The best detection flag from all detections of this source	
Fieldflag		The best field flag from all detections of this source	
DetFlag_band[0–4]		The best detection flag in each band, from all detections of the source in that band	
		<i>Count-rate and variability information</i>	
Rate_band[0–4]	ct s <sup>-1</sup>	The mean count-rate of the source in each band	yes
Counts_band[0–4]		The number of counts measured in the region of the source in each band	
BGCounts_band[0–4]		The number of counts in the background map in the region of the source in each band	
CF_band[0–4]		The count-rate correction factor ( $\kappa$ ) for the source in each band	
PvarPchiSnapshot_band[0–4]		The probability that the source is constant between snapshots in band 0–4, deduced via the Pearson's $\chi^2$ test	
PvarPchiObsID_band[0–4]		The probability that the source is constant between observations in band 0–4, deduced via the Pearson's $\chi^2$ test	
HR1		The HR1 hardness ratio	yes
HR2		The HR2 hardness ratio	yes
		<i>Flux and spectral information</i>	
GalNH	cm <sup>-2</sup>	The Galactic absorption column density in the direction of the source	
whichPow		The provenance of the summary spectral fields for the power-law model. 0=fixed spectrum, 1=HR-derived, 2=fitted spectrum	
whichAPEC		The provenance of the summary spectral fields for the APEC model. 0=fixed spectrum, 1=HR-derived, 2=fitted spectrum	
		<i>Summary spectral information</i> <sup>2</sup>	
PowECFO	erg cm <sup>-2</sup> ct <sup>-1</sup>	The counts-to-observed-flux energy conversion factor derived from the power-law spectrum	
PowECFU	erg cm <sup>-2</sup> ct <sup>-1</sup>	The counts-to-unabsorbed-flux energy conversion factor derived from the power-law spectrum	
PowFlux	erg cm <sup>-2</sup> s <sup>-1</sup>	The mean observed source flux derived from the power-law spectrum	yes
PowPeakFlux	erg cm <sup>-2</sup> s <sup>-1</sup>	The peak <sup>3</sup> observed source flux derived from the power-law spectrum	yes
PowUnabsFlux	erg cm <sup>-2</sup> s <sup>-1</sup>	The mean unabsorbed source flux derived from the power-law spectrum	yes
PowPeakUnabsFlux	erg cm <sup>-2</sup> s <sup>-1</sup>	The peak <sup>3</sup> unabsorbed source flux derived from the power-law spectrum	yes
APECECFO	erg cm <sup>-2</sup> ct <sup>-1</sup>	The counts-to-observed-flux energy conversion factor derived from the APEC spectrum	
APECECFU	erg cm <sup>-2</sup> ct <sup>-1</sup>	The counts-to-unabsorbed-flux energy conversion factor derived from the APEC spectrum	
APECFlux	erg cm <sup>-2</sup> s <sup>-1</sup>	The mean observed source flux derived from the APEC spectrum	yes
APECPeakFlux	erg cm <sup>-2</sup> s <sup>-1</sup>	The peak <sup>3</sup> observed source flux derived from the APEC spectrum	yes
APECUnabsFlux	erg cm <sup>-2</sup> s <sup>-1</sup>	The mean unabsorbed source flux derived from the APEC spectrum	yes
APECPeakUnabsFlux	erg cm <sup>-2</sup> s <sup>-1</sup>	The peak <sup>3</sup> unabsorbed source flux derived from the power-law spectrum	yes
		<i>Detailed spectral information</i>	
FixedPowECFO	erg cm <sup>-2</sup> ct <sup>-1</sup>	The counts-to-observed-flux energy conversion factor	

Table 7 — *Continued*

Field	Units	Description	Has errors? <sup>1</sup>
FixedPowECFU	erg cm <sup>-2</sup> ct <sup>-1</sup>	derived from the fixed power-law spectrum The counts-to-unabsorbed-flux energy conversion factor	
FixedPowFlux	erg cm <sup>-2</sup> s <sup>-1</sup>	derived from the fixed power-law spectrum The mean observed source flux derived	yes
FixedPowUnabsFlux	erg cm <sup>-2</sup> s <sup>-1</sup>	from the fixed power-law spectrum The mean unabsorbed source flux derived	yes
FixedAPECECF0	erg cm <sup>-2</sup> ct <sup>-1</sup>	The counts-to-observed-flux energy conversion factor derived from the fixed APEC spectrum	
FixedFixed APECECFU	erg cm <sup>-2</sup> ct <sup>-1</sup>	The counts-to-unabsorbed-flux energy conversion factor derived from the fixed APEC spectrum	
FixedAPECFlux	erg cm <sup>-2</sup> s <sup>-1</sup>	The mean observed source flux derived from the fixed APEC spectrum	yes
FixedAPECUnabsFlux	erg cm <sup>-2</sup> s <sup>-1</sup>	The mean unabsorbed source flux derived from the fixed APEC spectrum	yes
InterpPowECFO	erg cm <sup>-2</sup> ct <sup>-1</sup>	The counts-to-observed-flux energy conversion factor derived from the HR-derived power-law spectrum	
InterpPowECFU	erg cm <sup>-2</sup> ct <sup>-1</sup>	The counts-to-unabsorbed-flux energy conversion factor derived from the HR-derived power-law spectrum	
InterpPowFlux	erg cm <sup>-2</sup> s <sup>-1</sup>	The mean observed source flux derived from the HR-derived power-law spectrum	yes
InterpPowUnabsFlux	erg cm <sup>-2</sup> s <sup>-1</sup>	The mean unabsorbed source flux derived from the HR-derived power-law spectrum	yes
InterpPowNH	cm <sup>-2</sup>	The absorption column density derived from the HR-derived power-law spectrum	yes
InterpPowGamma	erg	The power-law photon index derived from the HR-derived power-law spectrum	yes
InterpAPECECF0	erg cm <sup>-2</sup> ct <sup>-1</sup>	The counts-to-observed-flux energy conversion factor derived from the HR-derived APEC spectrum	
InterpAPECECFU	erg cm <sup>-2</sup> ct <sup>-1</sup>	The counts-to-unabsorbed-flux energy conversion factor derived from the HR-derived APEC spectrum	
InterpAPECFlux	erg cm <sup>-2</sup> s <sup>-1</sup>	The mean observed source flux derived from the HR-derived APEC spectrum	yes
InterpAPECUnabsFlux	erg cm <sup>-2</sup> s <sup>-1</sup>	The mean unabsorbed source flux derived from the HR-derived APEC spectrum	yes
InterpAPECNH	cm <sup>-2</sup>	The absorption column density derived from the HR-derived APEC spectrum	yes
InterpAPECkT	keV	The plasma temperature derived from the HR-derived APEC spectrum	yes
P_pov		For sources without an HR-derived value, the probability of measuring the (HR1,HR2) value of this source if it had a power-law spectrum	
P_APEC		For sources without an HR-derived value, the probability of measuring the (HR1,HR2) value of this source if it had an APEC spectrum	
FittedPowECFO	erg cm <sup>-2</sup> ct <sup>-1</sup>	The counts-to-observed-flux energy conversion factor derived from the fitted power-law spectrum	
FittedPowECFU	erg cm <sup>-2</sup> ct <sup>-1</sup>	The counts-to-unabsorbed-flux energy conversion factor derived from the fitted power-law spectrum	
FittedPowFlux	erg cm <sup>-2</sup> s <sup>-1</sup>	The mean observed source flux derived from the fitted power-law spectrum	yes
FittedPowUnabsFlux	erg cm <sup>-2</sup> s <sup>-1</sup>	The mean unabsorbed source flux derived from the fitted power-law spectrum	yes
FittedPowNH	cm <sup>-2</sup>	The absorption column density derived from the fitted power-law spectrum	yes
FittedPowGamma	erg	The power-law photon index derived from the fitted power-law spectrum	yes
FittedPowChi		$\chi^2$ of the power-law spectral fit	
FittedPowDOF		Degrees of freedom in the power-law spectral fit	
FittedPowRedChi		$\chi^2_\nu$ in the power-law spectral fit	
FittedAPECECF0	erg cm <sup>-2</sup> ct <sup>-1</sup>	The counts-to-observed-flux energy conversion factor derived from the fitted APEC spectrum	
FittedAPECECFU	erg cm <sup>-2</sup> ct <sup>-1</sup>	The counts-to-unabsorbed-flux energy conversion factor derived from the fitted APEC spectrum	
FittedAPECFlux	erg cm <sup>-2</sup> s <sup>-1</sup>	The mean observed source flux derived from the fitted APEC spectrum	yes
FittedAPECUnabsFlux	erg cm <sup>-2</sup> s <sup>-1</sup>	The mean unabsorbed source flux derived from the fitted APEC spectrum	yes
FittedAPECNH	cm <sup>-2</sup>	The absorption column density derived from the fitted APEC spectrum	yes
FittedAPECkT	keV	The plasma temperature derived from the fitted APEC spectrum	yes



Table 7 — *Continued*

Field	Units	Description	Has errors? <sup>1</sup>
FittedAPECChi		$\chi^2$ of the APEC spectral fit	
FittedAPECDOF		Degrees of freedom in the APEC spectral fit	
FittedAPECRedChi		$\chi^2_{\nu}$ in the APEC spectral fit	
<i>Cross-correlation information</i> <sup>2</sup>			
Numxcorr		The number of matches in the external catalogs	
Numxcorr_slim		The number of matches in the external catalogs, excluding USNO-B1 and 2MASS	
isROSHRI		Whether the object does (1) or does not (0) match an object in the Rosat HRI catalog	
isROSPSPC		Whether the object does (1) or does not (0) match an object in the Rosat PSPC catalog	
is3XMM		Whether the object does (1) or does not (0) match an object in the 3XMM DR4 catalog	
isXMMSL1		Whether the object does (1) or does not (0) match an object in the XMMSL1 XMM-Newton Slew Survey	
isSwiftFT		Whether the object does (1) or does not (0) match an object in the Swift-FT catalog	
is1SWXRT		Whether the object does (1) or does not (0) match an object in the 1SWXRT catalog	
isXRTGRB		Whether the object does (1) or does not (0) match a cataloged XRT position of a Gamma Ray Burst	
isSDSSQSO		Whether the object does (1) or does not (0) match an object in the SDSS QSO DR 5 catalog	
is2MASS		Whether the object does (1) or does not (0) match a 2MASS source	
isUSNOB1		Whether the object does (1) or does not (0) match a USNO-B1 source	
isSIMBAD		Whether the object does (1) or does not (0) match a SIMBAD object	
xcorrIDs		A semi-colon delimited list of the identifiers of the matched sources	

**Note.** — <sup>1</sup> This is ‘no’ unless stated. For a field with errors, there are two error fields, *fieldname\_pos* and *fieldname\_neg*. <sup>2</sup>This is taken from the detailed spectral information, for the method given in the *whichPow* and *whichAPEC* fields. <sup>3</sup> The peak flux is derived using the summary ECF and the count-rate in of the brightest bin in the total band per-snapshot light curve.

**Table 8**  
Contents of the ‘Datasets’ catalog table

Field	Units	Description
ID		The unique identifier of the dataset. For observations this is the 11-digit ObsID. For stacked images it is the number of the image.
RA	degrees	Right Ascension of the field center (J2000)
Decl	degrees	Declination of the field center (J2000)
l	degrees	The Galactic longitude of the field center
b	degrees	The Galactic latitude of the field center
IsStacked		Indicates whether this is a stacked image (1) or not (0)
Exposure	s	The exposure time in the dataset
FieldBG_band[0–4]	ct s <sup>-1</sup> pixel <sup>-1</sup>	The mean background level in each band.
Numsrc_band[0–4]		The number of sources in this image in each band.
NumOK_band[0–4]		The number of <i>Good</i> and <i>Reasonable</i> sources in each band.
MedianNNDist_band[0–4]		The median distance between the sources in each band’s image.
Date_start	UT	The calendar date of the observation start
Date_stop	UT	The calendar date of the observation end
FieldFlag		The field flag
NumSnapshots		The number of snapshots in the dataset.
AstromErr	arcsec	The 90% confidence uncertainty in the astrometric solution for this field derived using 2MASS (Section 3.7).
StackedImage		For observations: the ID of the stacked image in which this observation is included. For stacked images: the IDs of any stacked images which overlap this one.

**Table 9**  
Contents of the ‘Detections’ catalog table

Field	Units	Description	Has errors?
DetID		A unique identifier for this detection	
ObsID		The unique 11-digit obsID of the dataset the detection occurred in.	
Band		The band in which the detection occurred, (0=total, 1=soft, 2=medium, 3=hard)	
DetFlag		The detection flag as an integer value	
img_x <sup>1</sup>	pixels	The x-location of the detection in XRT SKY coordinates	
img_y <sup>1</sup>	pixels	The y-location of the detection in XRT SKY coordinates	
OffAxis	arcmin	The mean off-axis angle of the detection in this observation	
RA	degrees	RA (J2000) of the detection using the star tracker astrometry	yes (statistical only)
Dec	degrees	Declination (J2000) of the detection using the star tracker astrometry	yes (statistical only)
Err90	arcsec	90% conf. radial position error, statistical+systematic	
RA_corr	degrees	RA (J2000) of the detection using 2MASS/XRT astrometry	
Dec_corr	degrees	Declination (J2000) of the detection using 2MASS/XRT astrometry	
Err90_corr	arcsec	90% conf. radial position error using 2MASS/XRT astrometry	
l	degrees	Galactic longitude of the detection	
b	degrees	Galactic latitude of the detection	
Counts		Number of events in the count-rate extraction region	
BGCts		The expected number of background events in the above region	
FieldExposure	s	The on-axis exposure of the dataset the detection is in.	
CF		The count-rate correction factor ( $\kappa$ )	
Rate	ct s <sup>-1</sup>	The count rate of the detection.	yes
ExposureFraction		The exposure time at the location of the detection divided by the on-axis exposure	
Cstat		The $\mathcal{C}$ value from the PSF fit	
Cstat_nosrc		The $\mathcal{C}$ value calculated with normalization=0	
LogLikelihood		The log-likelihood of the detection.	
SNR		The SNR of the detection	
Celldet_width	pixels	The size of the cell in which the detection was made.	
PSF_Radius	pixels	The radius of the circular region used in PSF fitting.	
PSF		Which PSF profile was selected by PSF fitting.	
ol_warn	magnitude	The number of magnitudes brighter than the warning level of any cataloged star within 30'' of the detection.	
FieldFlag		The flag associated with the dataset the detection is in.	
NNDist	arcsec	The distance to the nearest other detection in this image	
OKNNDist	arcsec	The distance to the nearest <i>Good</i> or <i>Reasonable</i> detection in this image.	
Num_snapshots		How many snapshots are in the image containing the detection.	
ImageBG	ct s <sup>-1</sup> pixel <sup>-1</sup>	The mean background level in the image, according to the background map.	
MergeRadius	pixels	The radius over which other detections in this image are assumed to be aliases of this detection.	
SourceID		The identifier of the unique 1SXPS source this to which this detection corresponds.	

**Note.** — <sup>1</sup> The SKY coordinate system for an image depends on the position information used process the raw XRT data, thus may not be the same for user-processed data.

**Table 10**  
Contents of the ‘Cross Correlations’ catalog table

Field	Units	Description
1SXPS_ID		The name of the 1SXPS source
ExtCat_ID		The name of the source in the external catalog
Catalog		The catalog containing the matched source
Distance	arcsec	The distance between the 1SXPS source and external catalog source
RA	degrees	The RA (J2000) of the source in the external catalog
Decl	degrees	The Declination (J2000) of the source in the external catalog
Err90	arcsec	The 90% confidence radial uncertainty in the external catalog position, including any systematic

## 6. VERIFICATION

We used simulations to verify the accuracy of the catalog, making these as realistic as possible by basing our simulations on real data. To do this we identified XRT observations of 2XMMiDR3 (Watson et al. 2009) fields, selected from that catalog all sources expected to contribute at least two events to the XRT image (assuming a typical AGN spectrum:  $N_H = 3 \times 10^{20} \text{ cm}^{-2}$ ,  $\Gamma = 1.7$ ), and visually inspected the XRT image to ensure that this list identified all objects in the field. We then passed this source list to our background map software, which created a model of the background in the real XRT image. This model then forms the basis of the simulations. We did this for a range of different positions on the sky and XRT exposure times.

To simulate an image we then used the background map just created, with the corresponding exposure map to measure the number of background counts,  $\mu_i$ , in each pixel  $i$ . For each pixel in the image we drew the number of events to simulate at random from a Poisson distribution with a mean of  $\mu_i$ . To add sources to the image we randomly drew from the  $\log N - \log S$  distribution of extragalactic sources from Mateos et al. (2008). For each source we randomized the position on the CCD, and then simulated  $C$  events, where  $C$  was drawn randomly from a Poisson distribution with a mean equal to the number of events expected from that source on-axis. These events were folded through the instrumental PSF to locate the specific pixel in which the photon fell. If the exposure map value at this pixel was less than the on-axis exposure value, a random number between 0 and 1 was generated. If this number was less than the fractional exposure of the pixel in question, the photon was added to the image, otherwise it was discarded. In this way we build up a realistic XRT image.

Although we had a discrete set of ‘seed’ images from which we could simulate data, by selectively excluding snapshots from those images, we were able to simulate a larger selection of exposure times than would be given simply by considering the seed images as unit elements. Similarly, we could simulate a range of background levels by multiplying the seed background map by an appropriate value. This allowed us to test our catalog software on a range of exposure times and background levels which mirrors that of the data in the catalog.

### 6.1. Background maps

To confirm that our background mapping was working correctly we simulated 400 images, with the background

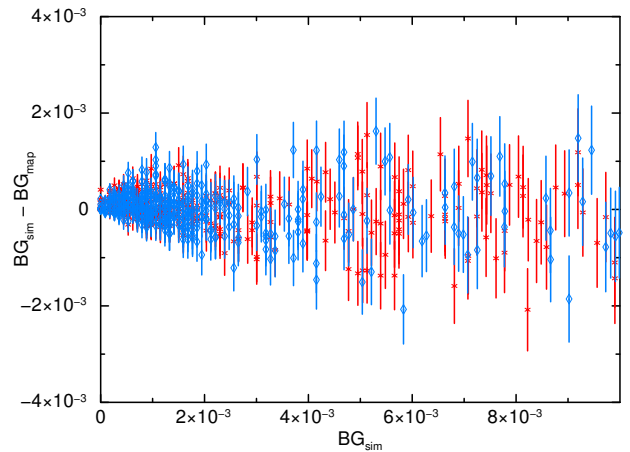


**Figure 8.** Comparison of the background measured directly from the simulated image ( $BG_{\text{sim}}$ ) with that measured from a background map ( $BG_{\text{map}}$ ) constructed from the simulated image. The red stars show the simulations with no sources included, the blue diamonds the simulations containing a source.

level and exposure time drawn at random from the distribution of those values seen in the catalog. Since these contain no sources, the true background level of each image can be measured directly. We then used our software to build a background map of these images and measured the background level from these maps, to compare with the true value. We measured the background by placing a circle of radius 60 pixels at a random location on the image and taking the mean value of all pixels in this circle with non-zero exposure. The same circle was used for an image and the corresponding background map, but a different circle was randomly placed for each simulation. The 60-pixel radius is much larger than the source extraction region used in the catalog, but is needed to reduce the magnitude of the Poisson uncertainty on the measurement of the simulated image. Fig. 8 shows the results of these tests, confirming that the background mapping tool performs well.

We performed a further 400 simulations independent of the set used above. This time a single source was added to the simulated image, although we also saved the source-less image, from which we measured the true background level. We then ran our source detection code on the image including the source. This detected the source and built a map of the underlying background. As Fig. 8 shows, the reconstructed background in these cases still accurately reflects the true value: a  $\chi^2$  test for the model  $BG_{\text{sim}} - BG_{\text{map}} = 0$  applied to these data gives  $\chi^2_\nu = 0.84$ , for 788 degrees of freedom.

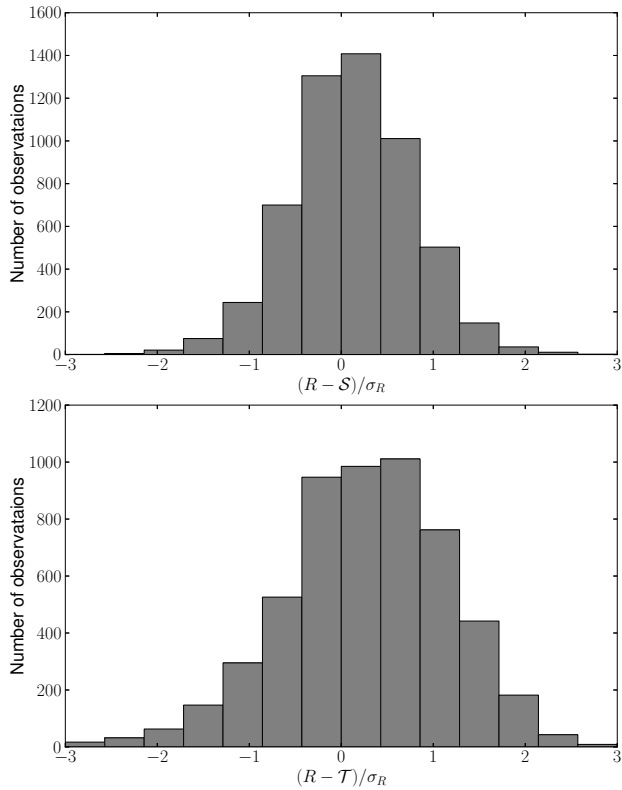


**Figure 9.** Histogram showing the accuracy of our count-rate reconstruction, based on simulation. *Top:* The difference between the measured and simulated source count rate, divided by the error on the measured value. *Bottom:* The difference between the measured and true source count rate, divided by the error on the measured value. The asymmetry in this plot is due to the Eddington bias.

### 6.2. Count-rate reconstruction

To test whether the source count-rate was adequately reconstructed, we performed a further 5,000 simulations, this time with multiple sources per image, as described in Section 6. For each source we drew the flux from the  $\log N - \log S$  distribution, multiplied it by the image exposure time and folded it through a typical AGN spectrum to obtain the expected number of XRT events,  $\mathcal{T}_c$ . To incorporate Poisson processes we then drew a number  $\mathcal{S}_c$  from a Poisson distribution with a mean of  $\mathcal{T}_c$ ; this ( $\mathcal{S}_c$ ) was the number of events which were actually put into the simulation. These events are folded through the PSF and exposure map (Section 6); the number which are actually included in the simulated image is  $A_c$ . Each of these numbers ( $\mathcal{T}_c, \mathcal{S}_c, A_c$ ) can be converted to a count-rate ( $\mathcal{T}, \mathcal{S}, A$ ) by dividing by the on-axis exposure time of the simulated image.

We ran the catalog software on these 5,000 simulated images to detect and characterize the sources, and then compared the count-rates thus obtained with the simulated count-rates. The top panel of Fig. 9 shows the distribution of  $(R - S)/\sigma_R$ , where  $R$  and  $\sigma_R$  are the source count-rate and error returned by the catalog software. This shows that our software is accurately reconstructing the count rates. The non-zero width of the distribution arises because of the PSF corrections and Poisson noise: if a source is located on the detector such that, on average, 30% of the simulated events are lost (i.e.  $A/S = 0.7$ )

then the catalog software (correctly) applies a correction of  $\kappa = 1/0.7$  to the measured count-rate. However due to Poisson processes, the values of  $A/S$  in the simulations show scatter around this mean value. Fig. 9 shows that this scatter is relatively narrow (a Gaussian fit has  $\sigma \sim 0.6$ ), and adding it to the count-rate uncertainty makes negligible difference to that value. Thus this effect can be safely neglected.

The bottom panel of Fig. 9 shows the distribution of  $(R - \mathcal{T})/\sigma_R$ . As can be seen, this distribution is significantly skewed with the catalog tending to overestimate the true count-rate. This is simply the result of the Eddington bias (Eddington 1940): if the true source count-rate is close to the detector limit then we detect those sources which Poisson noise makes appear brighter, but not those which are made fainter.

#### 6.2.1. Eddington bias

To explore the magnitude of the Eddington Bias in our data, we simulated a further 20,000 images, again with the exposure time and background level drawn at random from the distributions seen in the catalog, and with the source fluxes drawn from a  $\log N - \log S$  distribution. We then ran our catalog software on those images, recording both the ‘true’ count-rate from the simulation ( $\mathcal{T}$ ) and the count-rate  $R$  determined by our software. In Fig. 10 we show the distribution of the ratio  $R/\mathcal{T}$  as a function of how many simulated events there were ( $A_c$ ) for the source in question. This shows that (unsurprisingly) the Eddington bias is very strong for the faintest sources in the catalog, with the count-rates determined typically a factor of 2 too high. Although this bias lessens as we move to brighter sources, the distribution of rates recovered is still significantly asymmetric at  $A_c=20$ , however for sources with at least 30 events, the effect of the Eddington bias has all but disappeared.

#### 6.3. Variability test

We performed the Pearson’s  $\chi^2$  tests for variability on the sources in the 5,000 simulations created for Section 6.2. Since these sources are simulated with constant intensity (which is the null hypothesis of these tests) we expect that 10% of the sources will have a  $P < 0.1$  etc. Fig. 11 shows that this is the result obtained. This does not provide information on how strong variability has to be before it is detected, however this is a function of variability type, exposure, source brightness, light curve sampling etc. and should be determined on a per-source basis.

#### 6.4. Spectroscopy

The distribution of  $\chi^2_\nu$  from the power-law and APEC model spectral fits shows a clustering around  $\chi^2_\nu=1$  for both spectral models, as expected if those models are good representations of the data. About 25% of fits have  $\chi^2_\nu \gg 1$ , these represent cases where the simple spectral models we have used are not appropriate and more complex (e.g. multi-temperature) emission processes are likely involved. For those sources for which we have both a spectral fit with  $\chi^2_\nu < 1.5$  and an estimate of the spectral parameters derived from the hardness ratios, we show in Fig. 12 a histogram of the HR-Fit/Fit, for both the observed flux and the emission parameter.

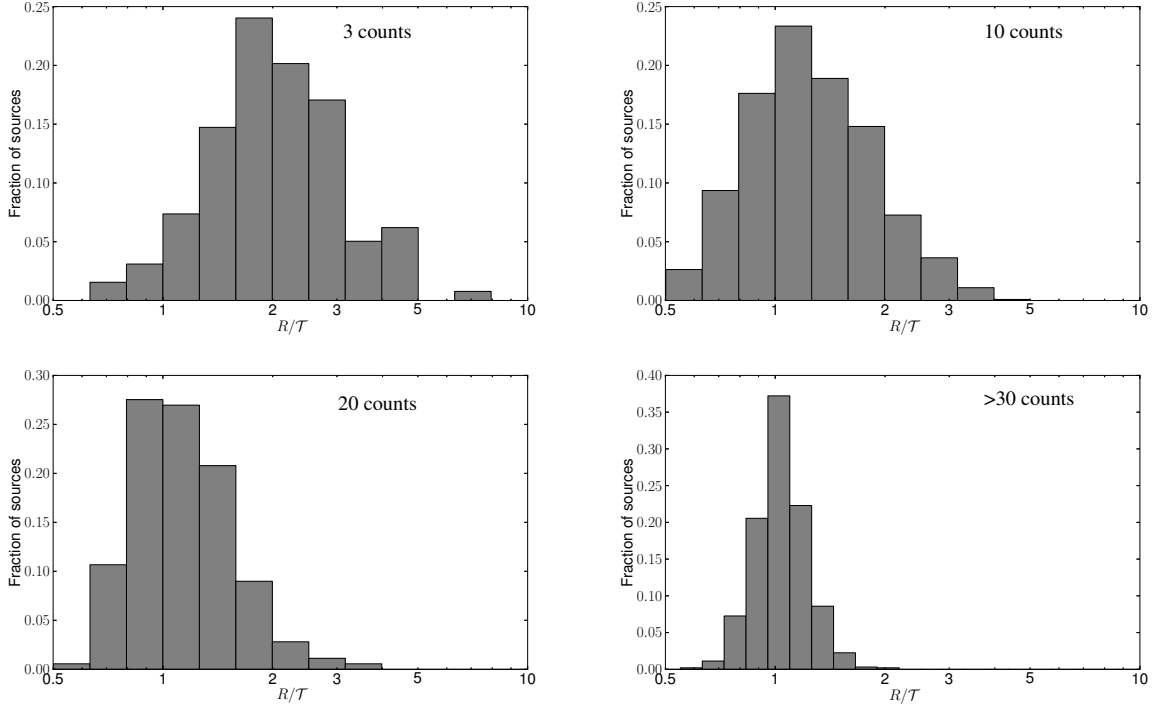


**Figure 10.** The effect of the Eddington Bias, showing the ratio of the measured count-rate to the true count-rate ( $R/T$ ) as a function of the number of simulated counts,  $A_c$ .

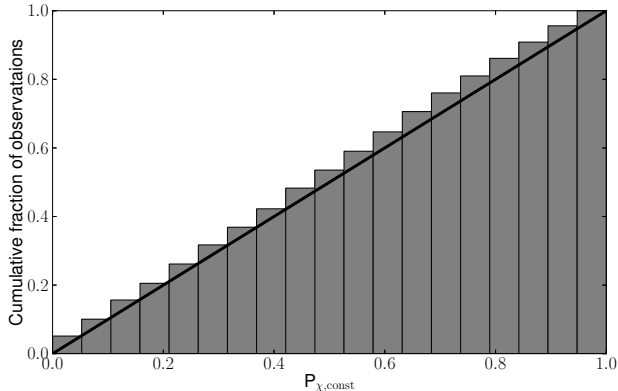


**Figure 11.** The cumulative probability distributions from the Pearson's  $\chi^2$  variability test applied to the constant sources in 5,000 simulated images. The black line shows the expected result which is well matched by the data.

This shows that the spectral parameters derived from the hardness ratios are reasonable.

#### 7. QUALITY FLAGS, FALSE POSITIVE RATE AND CATALOG COMPLETENESS

The quality flags described in Section 3.4 were calibrated such that the false positive rate in the catalog was 0.3%, 1% or 10% when *Good*, *Good* and *Reasonable*, or *Good*, *Reasonable* and *Poor* sources are included respectively. To calibrate these levels we again used simulations. Initially we performed a series of simulations of fixed exposure times (1,2,5,10,20,40 and 150 ks). We ran the catalog source detection software on each simulated image, and compared the list of detected sources with those simulated to determine the rate of false positives and therefore set the likelihood thresholds correspond-

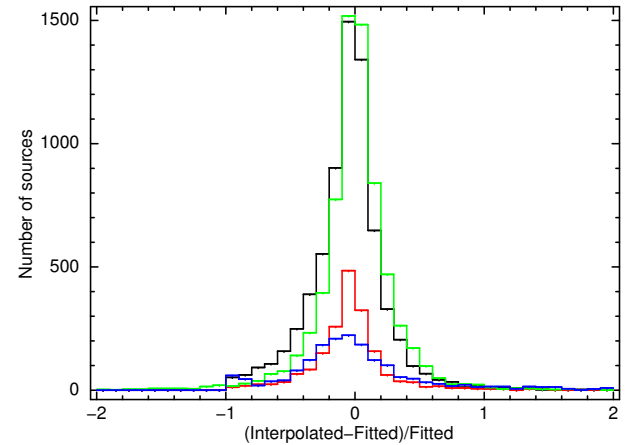


**Figure 12.** The difference between the spectral parameters derived from the hardness ratio and those from the spectral fit, divided by the spectrally-fitted value. Only sources where the spectral fit had  $\chi^2_{\nu} < 1.5$  are shown. *Black and red*: Observed flux from a power-law and APEC spectrum respectively. *Green*: Photon index from a power-law spectrum. *Blue*: Plasma temperature from an APEC spectrum.

ing to each quality flag. The false positive rate proved to be a function of exposure time, and we defined the quality flags accordingly. To test these flag definitions over a range of exposures and background levels more representative of the catalog than the discrete exposures use above, we ran a further 20,000 simulations, drawing the exposure time and background level at random from the distribution of these values in the catalog datasets. We found it necessary to reclassify some sources as *Bad* based on their positional errors. We also found that at exposures shorter than  $\sim 4$  ks, the false positive rate

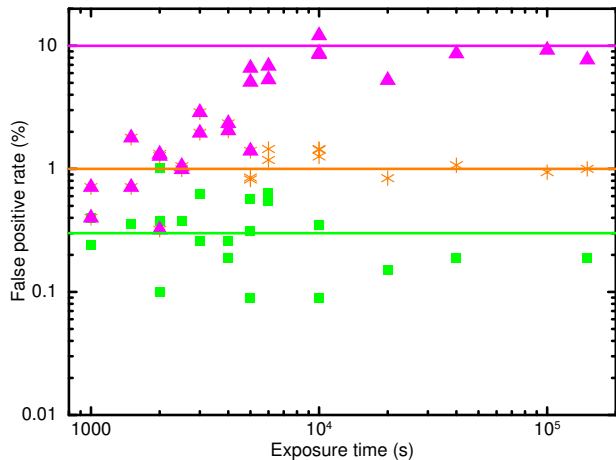


**Figure 13.** The false positive rate measured from the various simulation runs, as a function of exposure time. *Green:* *Good* sources. *Orange:* *Good* and *Reasonable* sources. *Magenta* all sources. The horizontal lines represent the 0.3%, 1% and 10% levels.

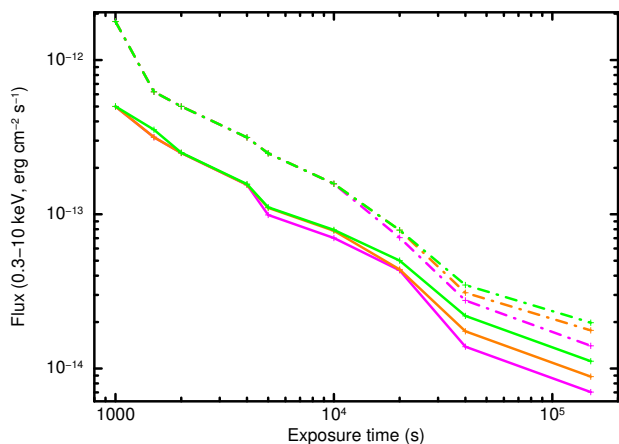


**Figure 14.** The completeness of our detection method as a function of exposure time and quality flag. The solid line is the 50% complete level, the dot-dashed line the 90% complete level. *Green:* *Good* sources. *Orange:* *Good* and *Reasonable* sources. *Magenta* all sources.

never rose above  $\sim 2\%$ , we therefore added a caveat that, for images shorter than 4 ks, the flag could only be *Good* or *Reasonable*. We ran a further 20,000 simulations to confirm that the results were stable. The formal definitions of the flags are given in Table 11; the false positive rate as a function of exposure time and quality flag is shown in Fig. 13.

We used the results of the simulations above to measure the fraction of simulated sources detected as a function of 0.3–10 keV source flux, exposure time and quality flag. Fig. 14 shows the result. The median exposure time of the observations in the catalog is 1.5 ks, at which our procedure is 50% complete at  $3 \times 10^{-13}$  erg cm $^{-2}$  s $^{-1}$ , and 90% complete at  $7 \times 10^{-13}$  erg cm $^{-2}$  s $^{-1}$ . For the stacked images, the median exposure time is 6 ks, at which our catalog is 50% complete at  $1 \times 10^{-13}$  erg cm $^{-2}$  s $^{-1}$ , and 90% complete at  $2 \times 10^{-13}$  erg cm $^{-2}$  s $^{-1}$ .

## 8. RESULTS AND DISCUSSION

Our catalog contains 151,524 unique sources of which 98,762 are in our highest quality ‘clean’ subsample (*Good*

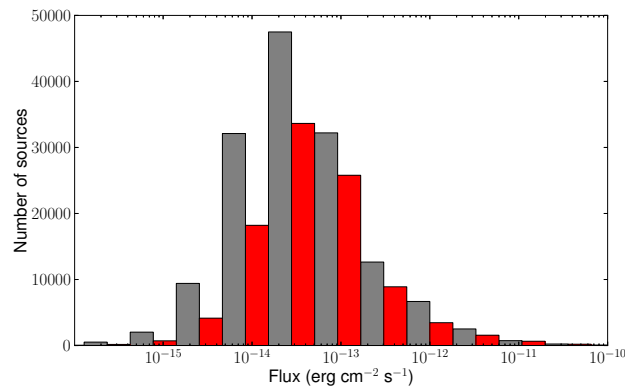


**Figure 15.** The distribution of the 0.3–10 keV mean observed flux (derived assuming a power-law spectrum) for the sources in our catalog. The gray bins are for all sources, the black bins (red in the electronic version) for those in the ‘clean’ subsample. The flux shown is taken from the spectral fit, where available; otherwise it comes from the hardness ratio interpolation, and if this is not available then from the fixed spectrum (see Section 4.2 for details).

and *Reasonable* sources only, excluding those in fields containing diffuse emission). Table 12 shows the breakdown of the sources according to the detection and field flags. The distribution of fluxes in the clean and total samples is shown in Fig. 15. Due to the effects of (in)completeness (Section 7) and the presence of the observation target object in our catalog, a  $\log N - \log S$  calculation cannot be deduced directly from this figure – see Mateos et al. (2008) for a detailed discussion of the issues involved.

Due to the observing strategy of *Swift*, our catalog gives a unique insight into variability on multiple timescales. Excluding GRBs, 28,906 sources are found to be variable at the  $3\text{-}\sigma$  level in at least one band or binning method. Fig. 16 shows the distribution of the  $\chi^2$  variability probability (Section 4.1) for the total-band light curves, GRBs have been excluded from this plot. A clear excess above the expected uniform distribution is seen at low probability of being constant, indicating a population of variable sources. Fig. 17 shows an example light curve of one of these sources, 1SXPS J192427.2+240925, which appears to be short-lived transient that was only visible for three snapshots. This object was found by searching for sources in the clean catalog sample that had a low probability of being constant and no counterpart found in the external catalog cross-correlation (apart from a USNO-B1 or 2MASS object). Further investigation revealed a single  $K = 16.06$  mag stellar object in the UKIDSS Galactic Plane Survey in the XRT error region. This object is not in the USNO-B1 catalog, which has a limiting sensitivity of  $V \sim 21$  mag. It thus seems likely that this object is an M dwarf star within 1 kpc, and that the XRT detected a coronal flare from it which lasted a few hours.

In Fig. 7 we showed the area of (HR1,HR2) space permitted by simple spectral models (a single absorber and emission component). Fig. 18 shows the distribution of 1SXPS sources in this space, revealing a significant number which do not lie within the range permitted by these simple models. Indeed  $\sim 14,300$  (9%) of all sources in the catalog are not consistent with the single-component power-law or APEC models, at the  $3\text{-}\sigma$  level. Fig. 18 also shows the distributions of the individual hardness ratios.

**Table 11**  
Definitions of the detection flags

Name	Definition
Good (=0)	$L > 18.52E^{-0.051}$
Reasonable (=1)	$L \leq 18.52E^{-0.051}$ ( $E < 4$ ks) $L > 36.32E^{-0.15}$ ( $4 \text{ ks} < E < 40$ ks) $L > 9.73E^{-0.024}$ ( $E \geq 40$ ks)
Poor (=2)	$L > 86.55E^{-0.29}$ ( $4 \text{ ks} < E < 26$ ks) $L > 3.47E^{0.027}$ ( $E \geq 26$ ks)
Bad <sup>1</sup>	$L < L_{\text{poor}}$ or any position err ( $\pm$ RA,Dec) $> 25''$
Value=8	As <i>Good</i> but in a region marked as containing artifacts.
Value=9	As <i>Reasonable</i> but in a region marked as containing artifacts.
Value=10	As <i>Poor</i> but in a region marked as containing artifacts.
Value=16	As <i>Good</i> but in a region marked as containing diffuse emission.
Value=17	As <i>Reasonable</i> but in a region marked as containing diffuse emission.
Value=18	As <i>Poor</i> but in a region marked as containing diffuse emission.

**Note.** —  $L$  is the source likelihood value, and  $E$  the exposure time in seconds.  
<sup>1</sup> *Bad* detections are not included in the catalog.

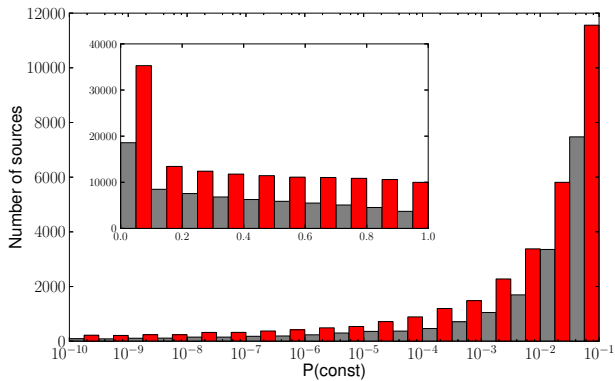


**Figure 16.** The distribution of the  $\chi^2$ -derived probability that a source is constant for the 1SXPS catalog sources, excluding GRB afterglows. The gray data are for inter-snapshot variability, the black bins (red in the electronic version) for inter-observation. The inset shows the entire probability range, over which a population of constant sources would show equal numbers of objects in each bin: the sharp spike at  $P < 0.1$  indicates a population of variable sources; the main plot shows a magnified view (with a logarithmic probability axis) of this region.

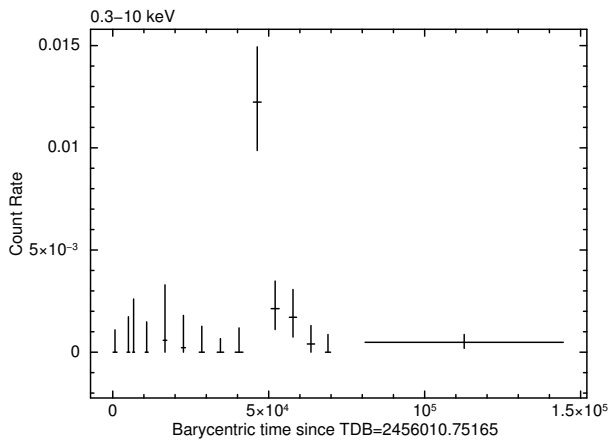


**Figure 17.** The total-band light curve of 1SXPS J192427.2+240925 with one bin per snapshot. This is a short-lived transient, newly discovered in the 1SXPS catalog.

**Table 12**  
The number of 1SXPS sources by flag values.

Flag Value	Num Sources
<b>Detection flags</b>	
<i>In fields flagged as OK</i>	
<i>Good</i>	69,967 (61%)
<i>Reasonable</i>	16,127 (14%)
<i>Poor</i>	27,904 (24%)
<i>In fields containing artifacts</i>	
<i>Good</i>	9,856 (42%)
<i>Reasonable</i>	2,812 (12%)
<i>Poor</i>	5,557 (23%)
Other <sup>1</sup>	5,433 (23%)
<i>In fields containing diffuse emission</i>	
<i>Good</i>	1,422 (10%)
<i>Reasonable</i>	455 (3%)
<i>Poor</i>	986 (7%)
Other <sup>1</sup>	11,005 (79%)
<i>In all fields</i>	
<i>Good</i>	81,245 (54%)
<i>Reasonable</i>	19,394 (13%)
<i>Poor</i>	34,447 (23%)
Other <sup>1</sup>	16,438 (11%)
<b>Field flags</b>	
OK	113,998 (75%)
Has artifacts	23,658 (16%)
Has diffuse emission	13,868 (9%)

**Note.** — <sup>1</sup> ‘Other’ refers to sources which lie within a region marked by manual screening, i.e. sources with detection flags of 8 or above. See Section 3.6.

### 8.1. Comparison with other catalogs

The combination of sensitivity and sky coverage of this catalog means it occupies the area of parameter space between the deep-and-narrow surveys such as 3XMM-DR4, 1CSC (Evans et al. 2010) and the *Chandra* BMW catalog (Romano et al. 2008); and the shallow-and-wide surveys such as the *Rosat* All-Sky Survey (Voges et al.



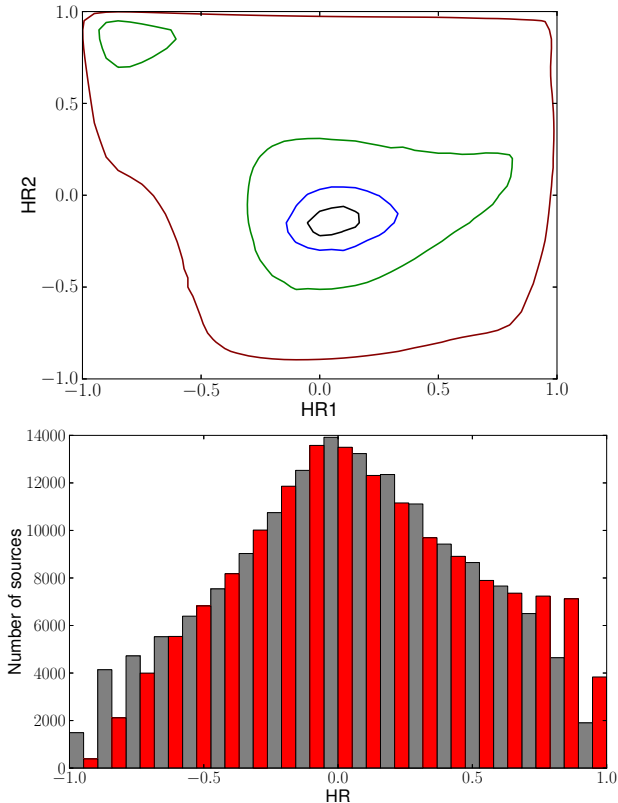


**Figure 18.** *Top:* Contour plot showing the (HR1,HR2) space occupied by the 1SXPS sources, after smoothing over the error range of the individual sources. The contours show the areas 25%,50%,75% and 90% of the peak density. *Bottom:* The distribution of the individual HR values. *Gray:* HR1, *Black:* HR2 (red in the electronic version).

1999) and the XMM Slew Survey (Saxton et al. 2008). The number of sources in the 1SXPS catalog with no counterpart in the set of catalogs shown in Table 6<sup>16</sup> is 68,638 (45%) sources from the full catalog, and 33,282 (34%) sources in the clean sample. In part this is simply due to the limited overlap between surveys: 31% of our fields have a 3XMM source within the field of view (including those undetected in our catalog), and 14% have an SDSS quasar in the field, giving an idea of the size of the overlap.

The fields of the earlier XRT catalogs of Puccetti et al. (2011) and D’Elia et al. (2013) are included in the sample we have used. We found many sources not in those catalogs, partly because we included more data, but mainly because of the difference in strategy between the catalogs. Puccetti et al. (2011) focused on only stacked

images of GRB fields (totaling 374 fields compared to our 7,343); D’Elia et al. (2013) used a much larger sample than Puccetti et al. (2011), similar in size to ours (35,011 observations compared to the 48,932 in our catalog<sup>17</sup>) however they used a higher SNR threshold than we did, and did not combine images thus limiting the sensitivity achieved. Our approach combines the advantages of both of these methods. Further, our improved detection system is significantly more sensitive than the XIMAGE-based approach employed in the earlier catalogs: for example simulations showed that in a 2 ks image for a source with a count-rate of  $0.004 \text{ ct s}^{-1}$  ( $\sim 2 \times 10^{-13} \text{ erg cm}^{-2} \text{ s}^{-1}$ , 0.3–10 keV) our system is 37% complete, which is 1.5 times as complete as the XIMAGE system; the same is true for a source of count-rate  $0.002 \text{ ct s}^{-1}$  ( $\sim 8 \times 10^{-14} \text{ erg cm}^{-2} \text{ s}^{-1}$ , 0.3–10 keV) in a 5 ks image; the false positive rates in the two approaches were found to be similar. This combination of factors explains the number of sources present in our catalog that were not found in the earlier XRT catalogs.

The X-ray sky is highly variable, as evidenced by Fig. 16, and to some extent all catalogs are biased in their contents towards sources in high states. For example Starling et al. (2011) used *Swift* to observe 94 unidentified X-ray sources from the XMM slew survey with much greater sensitivity than that survey but only detected 30% of the XMM objects. Nonetheless, this catalog, with its census of variability and useful combination of moderate exposure and moderate sensitivity, will serve as a useful baseline for future missions such as *eRosita* and provides valuable information on the nature of variable sources which will be part of the unresolved background for missions like *LOFT*.

## 9. ACKNOWLEDGEMENTS

PAE, JPO, APB, KLP, CP and CJM acknowledge support from the UK Space Agency. DNB and JAK acknowledge support from NASA contract NAS5-00136. GT acknowledges support from ASI-INAF grant I/004/11/0. We thank Simon Vaughan for helpful discussions during the preparation of this paper and Paul O’Brien for feedback on the manuscript. We also thank the anonymous referee for insightful and helpful comments. This work made use of data supplied by the UK Swift Science Data Center at the University of Leicester. This research has made use of the XRT Data Analysis Software (XRTDAS) developed under the responsibility of the ASI Science Data Center (ASDC), Italy. This research has made use of the SIMBAD database, operated at CDS, Strasbourg, France

<sup>16</sup> Excluding the 2MASS and USNO-B1 catalogs as the high spatial density of sources in these catalogs makes it hard to be certain of association with the 1SXPS source.

<sup>17</sup> The difference arising partly because our sample extends ten months after the D’Elia et al. (2013) sample, and partly because we set a lower limit of 100 s of PC mode data, where they use 500

**Table 13**  
The parameters for the  
PSF spoke model used  
in our background  
mapping tool

Parameter	Value
$u$	0.0574 <sup>1</sup>
$v$	0.1512 <sup>1</sup>
$R_{\min}$	5.6''
$R_{\text{pk}}$	42.4''
$R_{\max}$	238''
$N_{\text{pk}}$	0.21

**Note.** — <sup>1</sup>  $u$  and  $v$  are in units of half a phase, i.e. 15°.

## APPENDIX

### A. MODIFICATIONS TO THE PSF PROFILE

The standard PSF of the *Swift*-XRT was calibrated by Moretti et al. (2007) and is modelled as a radially-symmetric King function:

$$P(R) \propto \left[ 1 + \left( \frac{R}{R_C} \right)^2 \right]^{-\beta} \quad (\text{A1})$$

The real PSF shows deviations from this profile due to the presence of ‘spokes’ caused by the shadowing of light by the mirror support structure. Read et al. (2011) performed a comprehensive analysis of this effect for *XMM* and found that modulating the azimuthal variation of the PSF by a trapezoidal function, shown in Fig. 19, gave a good representation of the PSF spokes. We applied this model to the XRT, first modifying it to account for the smaller number of spokes in XRT data (12, compared to 16 for *XMM*); and then determined the function parameters by fitting the model to an XRT dataset. If the model depicted in Fig. 19 is  $f(\theta)$ , then the PSF is given by

$$P(R, \theta) = P(R) [1 + N(R)f(\theta)] \quad (\text{A2})$$

where  $N(R)$  reflects the fact that the strength of the spoking effect is a function of radius within the PSF. This is a simple function with four parameters:  $N_{\text{pk}}$ ,  $R_{\min}$ ,  $R_{\text{pk}}$  and  $R_{\max}$ .  $N(R)$  is given thus:

$$\begin{aligned} N(R) &= 0 && (R < R_{\min} \text{ or } R > R_{\max}) \\ N(R) &= \left( \frac{N_{\text{pk}}}{R_{\text{pk}} - R_{\min}} \right) (R - R_{\min}) && (R_{\min} < R < R_{\text{pk}}) \\ N(R) &= N_{\text{pk}} - \left( \frac{N_{\text{pk}}}{R_{\max} - R_{\text{pk}}} \right) (R - R_{\text{pk}}) && (R_{\text{pk}} \leq R \leq R_{\max}) \end{aligned} \quad (\text{A3})$$

(A4)

At  $R < R_{\min}$  or  $R > R_{\max}$   $N(R) = 0$ , at  $R_{\min} < R < R_{\text{pk}}$   $N(R)$  increases linearly to  $N_{\text{pk}}$  and then it decreases linearly again to 0 at  $R_{\max}$ .

A non-piled up point source would ideally be used to fit the PSF spoke parameters however this proved impossible. Each snapshot of *Swift* data has a slightly different pointing position and roll angle so to model the PSF spokes we had to use only a single snapshot of data. Pile up becomes an issue at around 0.6 ct s<sup>-1</sup> so single-snapshot images of non piled-up sources did not contain enough counts for us to perform a reliable fit to the relatively weak PSF spoke effect. We therefore used a brighter but piled up source, accepting that this will give us a model to the PSF spokes which is probably imperfect for non-piled-up source, but better than no model at all. The parameters of this fit are given in Table 13.

As well as adding in the PSF spokes it was sometimes necessary to incorporate out-of-time events into the background map when modeling sources. Out-of-time events are events detected while the CCD is being read out, spreading the  $y$ -position of those events along the entire column. Since the deadtime in PC mode is equal to 0.004 times the exposure time, the count-rate of out-of-time events in a given CCD column is simply 0.004 times the number of in-time events in that column. We estimate the latter value by reading the number of events in a 41 pixel high region centered on the source and then multiply this by 0.004 and divide it by 600 (the number of rows on the CCD). We then add the resultant value to the background map for every pixel on that row. We perform this for an 11 pixel wide region centered on the source. This is only done for sources brighter than 3 ct s<sup>-1</sup> since below this level OOT events are insignificant compared to the background.

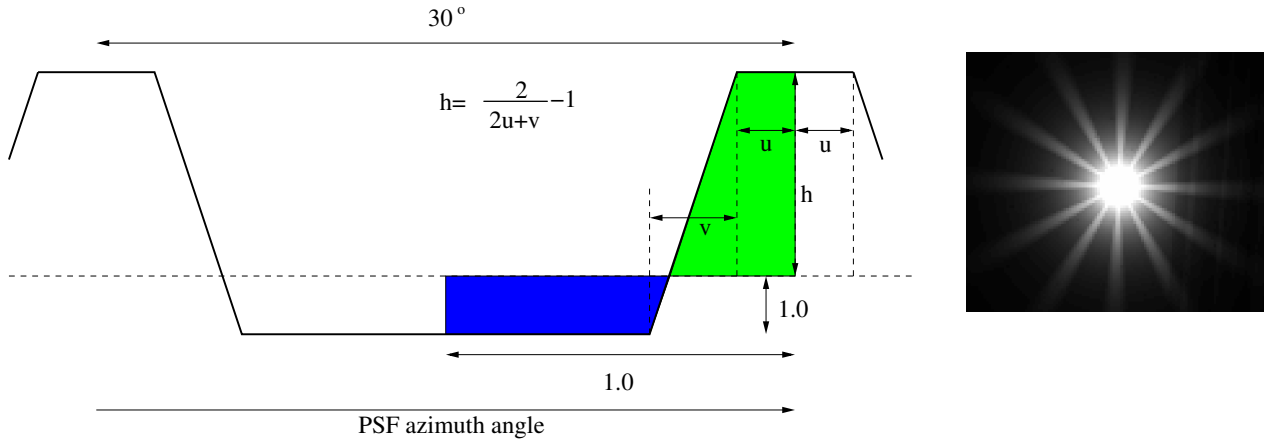


**Figure 19.** *Left:* the model for the PSF spokes, adapted from Read et al. (2011). The dashed horizontal line indicates the level of the PSF without modulation by the spokes. The function is constructed such that the dark and light gray areas have equal area (these are blue and green in the electronic version). The model is normalized such that the horizontal measurements are in units of half the inter-spoke distance, i.e.  $15^\circ$ , and the vertical measurements are in units of the maximum reduction in PSF brightness. The figure is not to scale. *Right:* an example PSF model including the spokes. The intensity is logarithmically scaled. The non-radial structure is caused by the exposure map.

## REFERENCES

- Abbey, T., Carpenter, J., Read, A., et al. 2006, in ESA Special Publication, Vol. 604, The X-ray Universe 2005, ed. A. Wilson, 943
- Burrows, D. N., Hill, J. E., Nousek, J. A., et al. 2005, Space Sci. Rev., 120, 165
- Butler, N. R. 2007, AJ, 133, 1027
- Calabretta, M. R. & Greisen, E. W. 2002, A&A, 395, 1077
- Cash, W. 1979, ApJ, 228, 939
- Churazov, E., Gilfanov, M., Forman, W., & Jones, C. 1996, ApJ, 471, 673
- D'Elia, V., Perri, M., Puccetti, S., et al. 2013, A&A, 551, A142
- Eddington, Sir, A. S. 1940, MNRAS, 100, 354
- Evans, I. N., Primini, F. A., Glotfelty, K. J., et al. 2010, ApJS, 189, 37
- Evans, P. A., Beardmore, A. P., Page, K. L., et al. 2009, MNRAS, 397, 1177
- Gehrels, N. 1986, ApJ, 303, 336
- Gehrels, N., Chincarini, G., Giommi, P., et al. 2004, ApJ, 611, 1005
- Goia, I. M., Maccacaro, T., Schild, R. E., et al. 1990, ApJS, 72, 567
- Goad, M. R., Tyler, L. G., Beardmore, A. P., et al. 2007, A&A, 476, 1401
- Greisen, E. W. & Calabretta, M. R. 2002, A&A, 395, 1061
- Høg, E., Fabricius, C., Makarov, V. V., et al. 2000, A&A, 363, 385
- Kennea, J. A., Burrows, D. N., Wells, A., et al. 2005, in Society of Photo-Optical Instrumentation Engineers (SPIE) Conference Series, Vol. 5898, Society of Photo-Optical Instrumentation Engineers (SPIE) Conference Series, ed. O. H. W. Sigmund, 341–351
- Kraft, R. P., Burrows, D. N., & Nousek, J. A. 1991, ApJ, 374, 344
- Mateos, S., Warwick, R. S., Carrera, F. J., et al. 2008, A&A, 492, 51
- Monet, D. G., Levine, S. E., Canzian, B., et al. 2003, AJ, 125, 984
- Moretti, A., Pagani, C., Cusumano, G., et al. 2009, A&A, 493, 501
- Moretti, A., Perri, M., Capalbi, M., et al. 2007, in Society of Photo-Optical Instrumentation Engineers (SPIE) Conference Series, Vol. 6688, Society of Photo-Optical Instrumentation Engineers (SPIE) Conference Series
- Park, T., Kashyap, V. L., Siemiginowska, A., et al. 2006, ApJ, 652, 610
- Pearson, K. 1900, Philosophical Magazine Series 5, 50, 157
- Protassov, R., van Dyk, D. A., Connors, A., Kashyap, V. L., & Siemiginowska, A. 2002, ApJ, 571, 545
- Puccetti, S., Capalbi, M., Giommi, P., et al. 2011, A&A, 528, A122
- Read, A. M., Rosen, S. R., Saxton, R. D., & Ramirez, J. 2011, A&A, 534, A34
- Romano, P., Campana, S., Mignani, R. P., et al. 2008, A&A, 488, 1221
- Samus, N. N., Kazarovets, E. V., Kireeva, N. N., Pastukhova, E. N., & Durlevich, O. V. 2010, Odessa Astronomical Publications, 23, 102
- Saxton, R. D., Read, A. M., Esquej, P., et al. 2008, A&A, 480, 611
- Schneider, D. P., Hall, P. B., Richards, G. T., et al. 2007, AJ, 134, 102
- Skrutskie, M. F., Cutri, R. M., Stiening, R., et al. 2006, AJ, 131, 1163
- Smith, R. K., Brickhouse, N. S., Liedahl, D. A., & Raymond, J. C. 2001, ApJ, 556, L91
- Starling, R. L. C., Evans, P. A., Read, A. M., et al. 2011, MNRAS, 412, 1853
- Tundo, E., Moretti, A., Tozzi, P., et al. 2012, A&A, 547, A57
- Ueda, Y., Ishisaki, Y., Takahashi, T., Makishima, K., & Ohashi, T. 2005, ApJS, 161, 185
- Voges, W., Aschenbach, B., Boller, T., et al. 1999, A&A, 349, 389
- Wald, A. & Wolfowitz, J. 1940, The Annals of Mathematical Statistics, 11, 147
- Warren, Jr., W. H. & Hoffleit, D. 1987, in Bulletin of the American Astronomical Society, Vol. 19, Bulletin of the American Astronomical Society, 733
- Watson, M. G., Schröder, A. C., Fyfe, D., et al. 2009, A&A, 493, 339
- Willingale, R., Starling, R. L. C., Beardmore, A. P., Tanvir, N. R., & O'Brien, P. T. 2013, MNRAS, 431, 394
- Wilms, J., Allen, A., & McCray, R. 2000, ApJ, 542, 914